### Title

Drosophila Mtm and class II PI3K coregulate a PI(3)P pool with cortical and endolysosomal functions.




### Journal

The Journal of cell biology, 190(3)

### ISSN

0021-9525



### Authors

Velichkova, Michaella
Juan, Joe
Kadandale, Pavan
et al.



### Publication Date

2010-08-01

### DOI

10.1083/jcb.200911020

Peer reviewed

# *Drosophila* Mtm and class II PI3K coregulate a PI(3)P pool with cortical and endolysosomal functions

Michaella Velichkova,[1] Joe Juan,[1] Pavan Kadandale,[1] Steve Jean,[1] Inês Ribeiro,[1] Vignesh Raman,[1] Chris Stefan,[2] and Amy A. Kiger[1]

[1]Section of Cell and Developmental Biology, University of California, San Diego, La Jolla, CA 92093
[2]Weill Institute for Cell and Molecular Biology, Cornell University, Ithaca, NY 14853

Reversible phosphoinositide phosphorylation provides a dynamic membrane code that balances opposing cell functions. However, in vivo regulatory relationships between specific kinases, phosphatases, and phosphoinositide subpools are not clear. We identified *myotubularin* (*mtm*), a *Drosophila melanogaster* MTM1/MTMR2 phosphoinositide phosphatase, as necessary and sufficient for immune cell protrusion formation and recruitment to wounds. Mtm-mediated turnover of endosomal phosphatidylinositol 3-phosphate (PI(3)P) pools generated by both class II and III phosphatidylinositol 3-kinases (*Pi3K68D* and *Vps34*, respectively) is needed to down-regulate membrane influx, promote efflux, and maintain endolysosomal homeostasis. Endocytosis, but not endolysosomal size, contributes to cortical remodeling by *mtm* function. We propose that Mtm-dependent regulation of an endosomal PI(3)P pool has separable consequences for endolysosomal homeostasis and cortical remodeling. *Pi3K68D* depletion (but not *Vps34*) rescues protrusion and distribution defects in *mtm*-deficient immune cells and restores functions in other tissues essential for viability. The broad interactions between *mtm* and class II *Pi3K68D* suggest a novel strategy for rebalancing PI(3)P-mediated cell functions in MTM-related human disease.

## Introduction

Different phosphoinositide phosphates (PIPs) under the control of kinase/phosphatase regulation are enriched in distinct membranes and direct localized cell functions (Di Paolo and De Camilli, 2006). A confounding issue in deciphering the relationship between PIP regulation and function is that different members of kinase/phosphatase families exhibit the same PIP selectivity in vitro, yet when mutated in vivo, are associated with specific diseases (Vicinanza et al., 2008). Myotubularins (MTMs) encode conserved phosphoinositide 3-phosphate phosphatases selective for phosphatidylinositol 3-phosphate (PI(3)P) and PI(3,5)$P_2$ (Taylor et al., 2000; Berger et al., 2002; Kim et al., 2002) found as large gene families in metazoans (15 human, 7 fly, and 1 yeast; Laporte et al., 1998; Robinson and Dixon, 2006; Tosch et al., 2006). MTM1 is associated with human myotubular myopathy (Laporte et al., 1996), whereas the closely related MTMR2 is associated with Charcot-Marie-Tooth neuropathy (Bolino et al., 2000), both characterized by distinct morphological defects. In cell cultures, MTM1 and MTMR2 were detected on endosomes and isolated in complexes with the class III phosphatidylinositol 3-kinase (PI3-kinase) Vps34 (Tsujita et al., 2004; Cao et al., 2007, 2008), which is consistent with MTM in vitro substrates and suggesting coordinated regulation of localized PIP pools. However, the identity of the PIPs that require MTM1/MTMR2 in cells and the relationship to requirements in animals remain largely unexplored.

Membrane influx from distinct PI(3)P pools converges at late endosomes (Simonsen et al., 2001; Lindmo and Stenmark, 2006). PI(3)P is highly enriched on early endosomes (Gillooly et al., 2000) with well-described roles defined by conserved Vps34 functions (Schu et al., 1993). The recruitment of proteins

Correspondence to Amy A. Kiger: akiger@ucsd.edu

Abbreviations used in this paper: ecdysone, 20-hydroxyecdysone; F-actin, filamentous actin; MTM, myotubularin; PI3-kinase, phosphatidylinositol 3-kinase; PI(3)P, phosphatidylinositol 3-phosphate; PIP, phosphoinositide phosphate; TIFF, tagged image file format; UAS, upstream activating sequence; WT, wild type.



The Rockefeller University Press $30.00
J. Cell Biol. Vol. 190 No. 3 407–425
www.jcb.org/cgi/doi/10.1083/jcb.200911020

with PI(3)P-binding domains mediate protein sorting, membrane transport, homotypic and heterotypic fusion with lysosomes, and endolysosomal maturation (Wurmser and Emr, 1998; Lindmo and Stenmark, 2006; Mima and Wickner, 2009; Saftig and Klumperman, 2009). PI(3)P is also considered central to autophagy, as demonstrated by an essential role for Vps34 in autophagosome formation and delivery of cytoplasmic content to endolysosomes for degradation (Kihara et al., 2001; Juhász et al., 2008; Simonsen and Tooze, 2009). Additionally, PI(3)P pools generated by class II PI3-kinase isoforms restricted to metazoans (MacDougall et al., 1995) are implicated in functions at the plasma membrane (MacDougall et al., 2004; Maffucci et al., 2005; Falasca and Maffucci, 2007; Falasca et al., 2007; Wen et al., 2008; Srivastava et al., 2009), although with unknown endosomal roles. Homeostasis of late endosomes depends on a balance between membrane influx and efflux that leads to diverging retrograde and recycling routes (Johannes and Popoff, 2008; Grant and Donaldson, 2009). Specificity in endocytic trafficking is emerging as a key site of regulation for many cellular and disease states (Gonzalez-Gaitan, 2008; Mosesson et al., 2008). Thus, specific kinases and phosphatases may be dedicated to the synthesis and turnover of PI(3)P subpools that intersect at endosomes.

*Drosophila melanogaster* presents an ideal system to elucidate metazoan PIP regulation and the functional nexus between specific PIP regulators, substrate identities, and their cell developmental roles (Hafen, 2004). We demonstrate an important functional relationship between the single *Drosophila* MTM1/MTMR2 orthologue Mtm and the class II PI3-kinase Pi3K68D. We show that Mtm and Pi3K68D coregulate PI(3)P to mediate endolysosomal flux and cortical dynamics in hemocytes, insect immune cells, and essential roles in animals.

## Results

### Identification of mtm function that promotes cell remodeling

Remodeling of the cell cortex, an integrated result of cytoskeletal and membrane reorganization, is important for diverse cell functions. To identify genes required for cellular remodeling, we performed RNAi of *Drosophila* kinases and phosphatases for functions that affect a hormone-induced cell shape change in 20-hydroxyecdysone (ecdysone)–responsive hemocyte-derived $Kc_{167}$ cells (Fig. 1, A and B; and Fig. S1; Echalier, 1997). Depletion of *mtm* inhibited remodeling from a round to an elongated cell shape, and instead, cells remained round without microtubule bipolar protrusions (Fig. 1, B′ and C). In the absence of ecdysone, the *mtm*-depleted cells exhibited normal morphology, growth, and survival (Fig. 1, D and E; and Fig. S2), as well as normal cell survival and hallmarks of hormone reception upon ecdysone addition, including increased cell size and up-regulated levels of ecdysone receptor (Fig. S2). The ecdysone-induced *mtm* RNAi cells inappropriately retained a uniform band of cortical filamentous actin (F-actin), which when destabilized, uncovered the ability for microtubule polymerization (Fig. 1 F). Overexpression of wild-type (WT) *mtm* cDNA drove the elongation of bipolar $Kc_{167}$ cells in the absence of ecdysone addition (70.3% GFP:Mtm bipolar cells; Fig. 1 G). These results suggest an *mtm* function separable from ecdysone reception that promotes F-actin reorganization and cortical remodeling.

### Essential tissue-specific roles for conserved mtm phosphoinositide phosphatase

To investigate the significance of an *mtm* function for cell remodeling in animal development, we generated *Drosophila* mutant alleles (Fig. 2 A). A point mutation within the catalytic $CX_5R$ motif ($mtm^{z2\text{-}4747}$) and null excision alleles ($mtm^{\Delta 77}$ and $mtm^{\Delta 210}$) exhibited larval lethality, indicating an essential requirement for *mtm* phosphatase activity (Fig. 2, A and B). Targeted expression of *mtm* RNAi hairpins uncovered requirements in specific tissues, including independent roles likely to act in muscle and hemocytes (Table S1). Coexpression of either fly *mtm* or human *MTMR2* cDNAs rescued RNAi-induced animal lethality, demonstrating *mtm* knockdown specificity and functional conservation with the human gene (Fig. 2 B and Table S1).

### Mtm is necessary and sufficient for immune cell protrusion formation

An *mtm*-dependent hemocyte function suggested unexplored roles for MTMs in immune cells (Fig. 2 B). As predicted from $Kc_{167}$ cells, *mtm* function impaired cortical remodeling in hemocytes. In postembryonic stages, hemocytes exist as round cells distributed in the body cavity and as spread cells in sessile populations adherent to the body wall (Lanot et al., 2001). Upon dissection from larvae, primary hemocytes undergo remodeling from a round to spread cell shape, exhibiting F-actin–rich radial protrusions that dynamically extend and retract perpendicular to the periphery (Fig. 2, C and G; and Video 1). In contrast, both *mtm* mutants and hemocyte-autonomous depletion resulted in spread cells that completely lacked radial protrusions (control, 3.8%; *mtm* mutant cells, 76.8–99.5%; Fig. 2, D, E, and G), even with knockdown induced in larvae (Fig. 2 H). Mutant cells exhibited smooth or ruffled edges, often a larger cell footprint, and a broad band of circumferential F-actin and SCAR protein (Fig. 2 I; Zallen et al., 2002). The *mtm*-depleted cells exhibited a dynamic cell cortex, and although short protrusions appeared, they abnormally moved radially along the periphery (Video 1). Strikingly, *mtm* overexpression in WT hemocytes led to an opposite phenotype of excessive radial protrusions (control, 4.1%; *mCherry*:*mtm* cells, 62.2%; Fig. 2, F and G).

### Mtm function in vivo is important for immune cell distribution and recruitment to wounds

Consistent with a specific role for *mtm* affecting cell shape, larval hemocyte number, cell viability, and differentiation were unaffected in *mtm* mutants (Fig. 3, A–D). Although similar numbers of sessile hemocytes were observed for both, either *mtm* knockdown or WT *mtm* cDNA expression led to aberrantly clumped or dispersed hemocyte distribution, respectively (Fig. 3, C and D). Defects in cell morphogenesis and dispersion could disrupt hemocyte recruitment abilities needed in immune and wounding responses (Williams, 2007; Babcock et al., 2008).

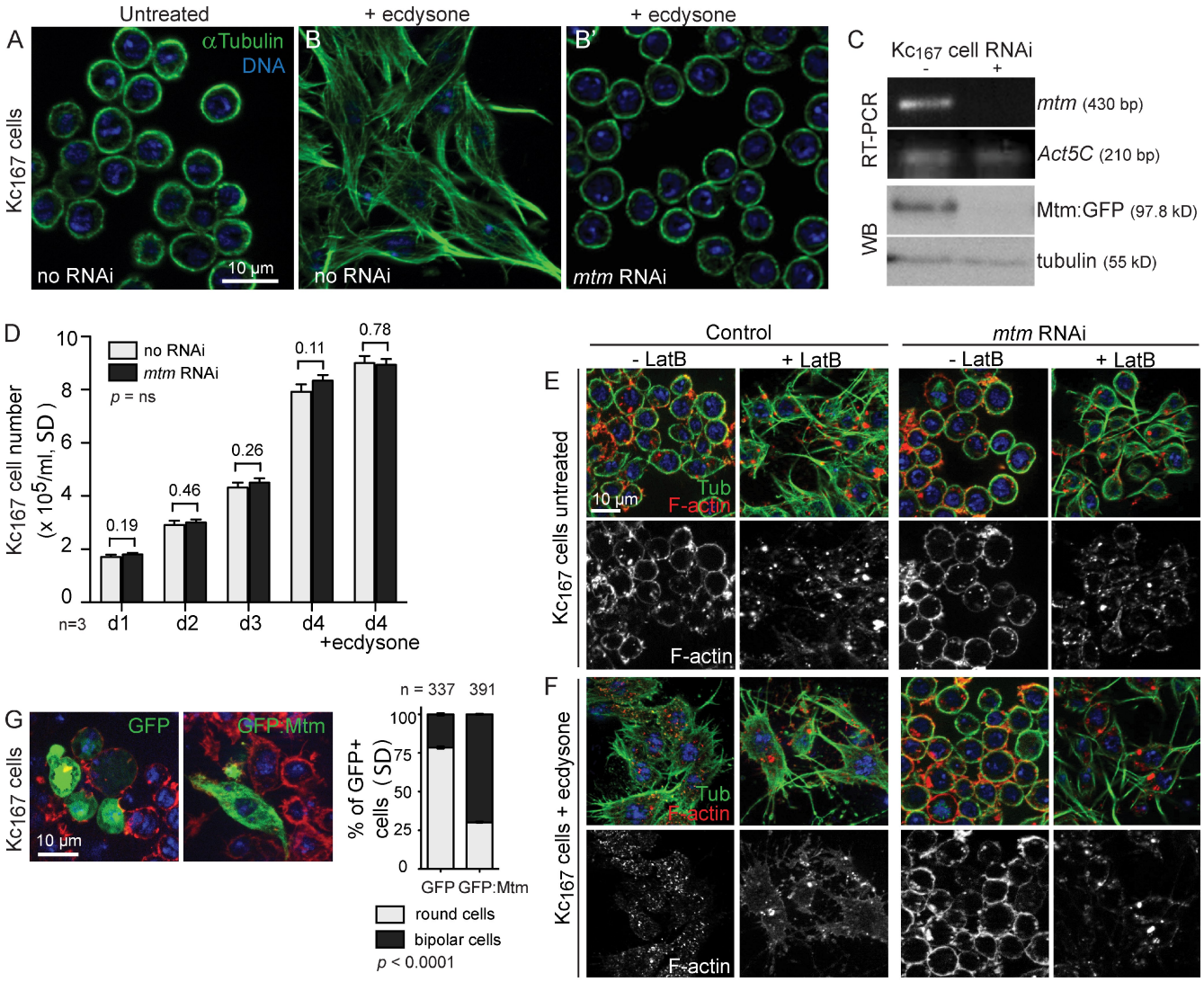


Figure 1. ***mtm* promotes remodeling of cell shape.** (A and B) Microtubules in *Drosophila* $Kc_{167}$ cells reveal normal round (A) and bipolar (B)-shaped cells 1 d after ecdysone. (B′) *mtm* RNAi inhibited ecdysone-induced cell elongation. (C) RNAi depletion of *mtm* transcript and Mtm-GFP (anti-GFP). WB, Western blot. (D) Cell numbers 1–4 d after RNAi. (E) Normal morphology of *mtm*-depleted cells in absence of ecdysone. (E and F) Latrunculin B (+LatB) destabilized F-actin (red) and permitted microtubule protrusions (green) in untreated (E) and ecdysone-treated (F) *mtm* RNAi cells. (G, right) GFP:Mtm induced cell elongation in absence of ecdysone. (left) GFP cells remained round. Percentage of transfected round or bipolar-shaped cells. Error bars indicate mean ± SD.

Puncture wounds in WT larvae led to the recruitment of 32.3 ± 4.9 hemocytes at the clot 6 h after wounding (Fig. 3, E and F). In contrast, either *mtm* knockdown or overexpression in hemocytes, corresponding to lack of or ectopic cell protrusions, respectively (Fig. 2, E and F), disrupted hemocyte numbers at wounds (10.2 ± 3.2; 9.7 ± 2.7 cells; Fig. 3, E and F). Altogether, *mtm* function is both necessary and sufficient for the formation of hemocyte protrusions, with in vivo consequences on hemocyte dispersion and efficient recruitment to wounds.

## Mtm is necessary and sufficient for homeostasis of endolysosomes

To pinpoint *mtm* cellular mechanisms, we investigated the identity of the Mtm functional PIP substrate by addressing effects on specific PIP-containing membranes, regulation of PIP levels, and distributions and genetic requirement for specific PIP pools. We first tested whether *mtm* function affected specific endosomal or autophagic membrane identities. Rab5-containing early endosomes, known sites of abundant PI(3)P synthesis (Wucherpfennig et al., 2003), were unaltered in morphology and number, although with a slight decrease in size detected in *mtm* RNAi cells (Fig. 4, A, A′, and H). In contrast, enlarged GFP:Rab7 and GFP:LAMP compartments suggested an *mtm*-dependent function for late endosome–lysosomes (endolysosomes; Saftig and Klumperman, 2009), which are known sites of transition from PI(3)P to $PI(3,5)P_2$ synthesis (Fig. 4, B–D′ and H; Di Paolo and De Camilli, 2006). Giant compartments detected with acidic pH-sensitive LysoTracker were associated with late endolysosomal proteins (Fig. 4, D′–G′) and more than threefold enlarged (Fig. 4 H), indicating normal traffic and function of lysosomal $H^+$-ATPases despite increased organelle size. The LysoTracker compartment in *mtm*-depleted cells further increased to nearly fourfold in size upon ecdysone addition, indicating an *mtm* function separable from ecdysone reception

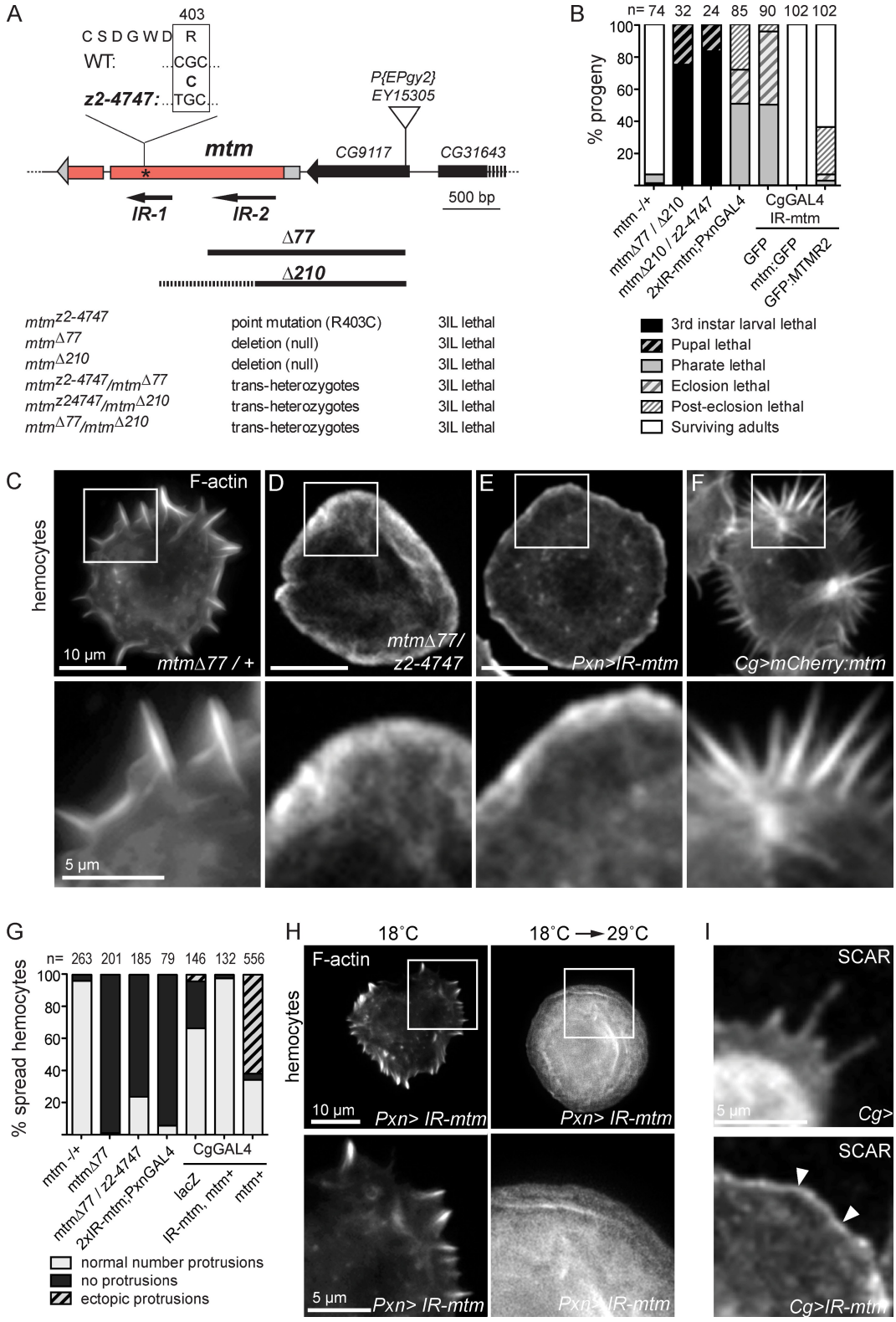


Figure 2. ***mtm* promotes hemocyte protrusions and essential roles in *Drosophila*.** (A) Larval lethal *mtm* mutant alleles: *z2-4747* mutation in $CX_5R$ catalytic motif, *Δ77* and *Δ210* deletions, and *UAS-IRmtm* RNAi hairpins. (B) Percentage of lethal progeny for *mtm* alleles or hemocyte-targeted RNAi (PxnGAL4; CgGAL4) rescued to viability with *mtm* or human *MTMR2* cDNA. (C–F) F-actin in primary hemocytes (top) and zoom of cell edges (bottom). (C) Normal radial protrusions in $mtm\Delta77/+$. (D and E) Lack of protrusions in $mtm^{\Delta77}/mtm^{z2\text{-}4747}$ and hemocyte *mtm* RNAi. (F) Increased number of protrusions in *mtm* overexpression. (G) Percentage of hemocytes with normal, no, or ectopic protrusions. (H, right) Lack of hemocyte protrusions with 1-d induced *mtm* RNAi (18 to 29°C shift). *IR-mtm/+; Pxn-GAL4/+*. (I) SCAR protein in control (top) and enriched along cell cortex in *mtm*-depleted hemocytes (bottom, arrowheads; *Cg-GAL4/IRmtm*). Boxed areas are shown at magnified views in the panels below.

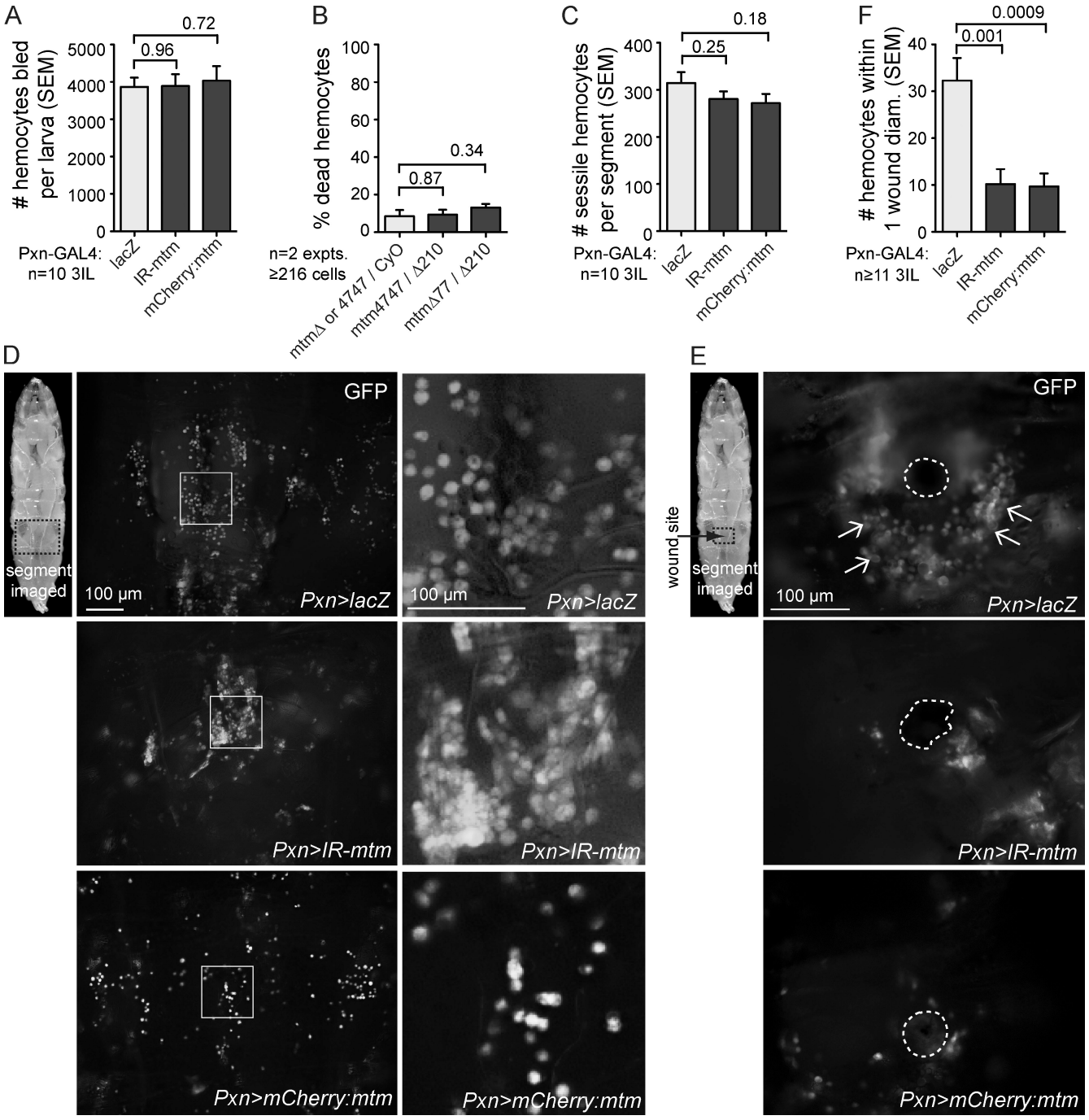


Figure 3. ***mtm* disrupts hemocyte distribution and recruitment to larval wounds.** (A–C) *mtm* function did not affect the number of bled hemocytes (A), percentage of dead or dying hemocytes (B; see Materials and methods; genotypes as shown), or number of sessile hemocytes per segment of third instar larva (C). (D) GFP+ hemocytes imaged in dorsal segment: control (top), *mtm* RNAi (middle), and *mtm* expression (bottom). Boxes represent the higher magnified views at right. (E) GFP+ hemocytes (arrows) recruited 6 h after wounding to puncture sites in dorsal segments. (F) Either *mtm* depletion or expression reduced the number of hemocytes within one-wound diameter. (A and C–F) *IR-mtm/+* or *mCherry:mtm/+* with *Pxn-GAL4, UAS-GFP/+*. Error bars indicate SEM.

that may impact membrane flux (Fig. S2 G). The size of LysoTracker-positive organelles was restored with *mtm* cDNA expression in *mtm*-depleted hemocytes (Fig. 4 G), whereas the size further decreased with expression in WT hemocytes (Fig. 4, I–J′). Ultrastructural analysis in *mtm*-depleted $Kc_{167}$ cells confirmed an increased cell area of secondary lysosomes (lamellar bodies and autophagolysosomes; Sunio et al., 1999). Secondary lysosomes were evident both in small clusters and as single, giant membrane–delimited structures (Fig. 4, K–M), which is consistent with transport, tethering, and fusion of late endosomes with lysosomes. The ultrastructure also revealed an increase in size and frequency of both single and double membrane-delimited electron-lucent compartments (Fig. 4, K′ and N–P). Double-membrane structures were characteristic of autophagosomes (Fig. 4, O and O′), organelles involved in the PI(3)P-dependent process of autophagy (Juhász et al., 2008;

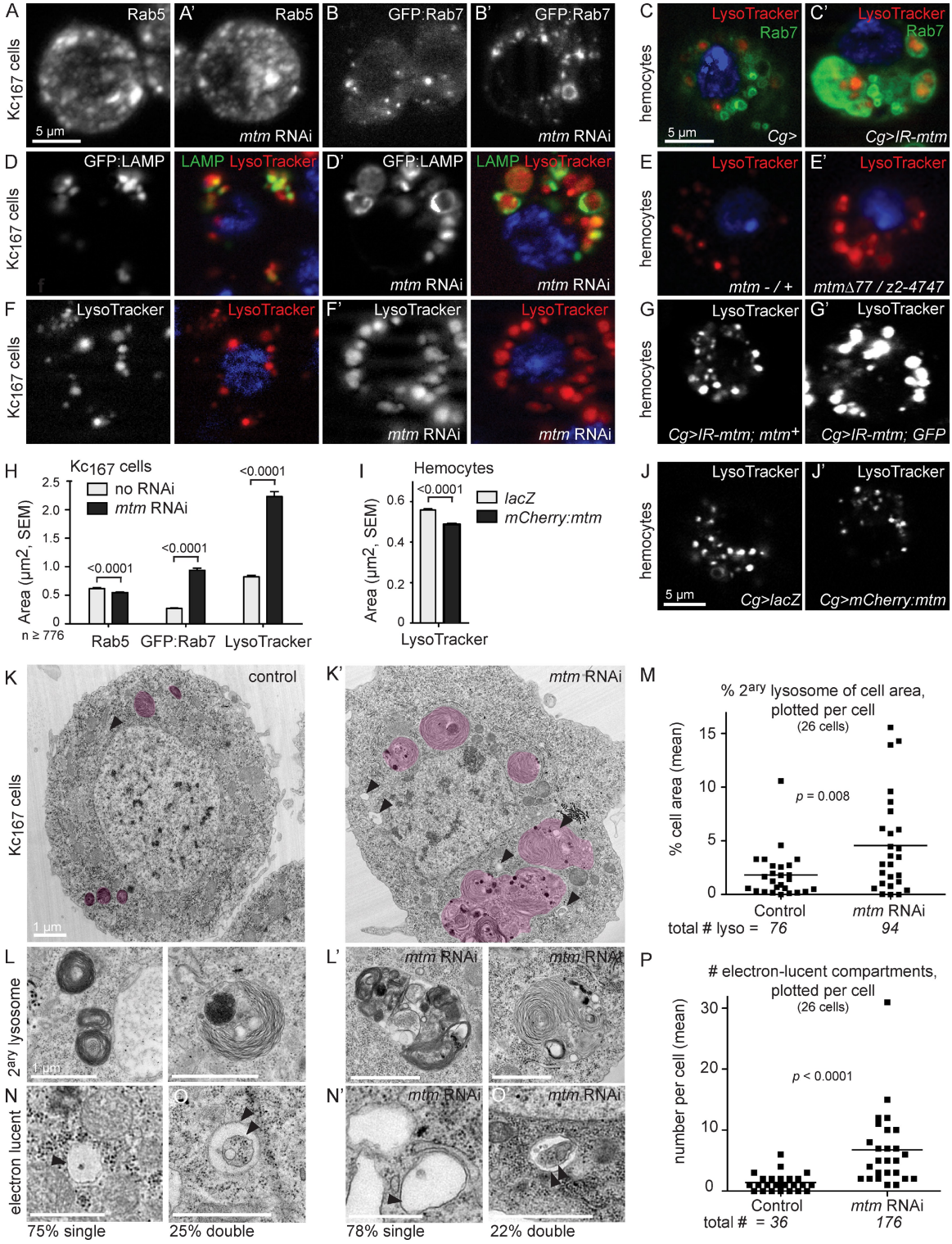


Figure 4. ***mtm* controls endolysosome homeostasis.** (A′–B′, C′, D′, E′, F′, and G′) *mtm* is necessary and sufficient to restrict size of acidified endolysosomes in $Kc_{167}$ cells (A′–B′, D′, and F′) and primary hemocytes (C′, E′, and G′). (A′ and B′–C′) Normal early endosomes (A′; anti-Rab5) and enlarged and convoluted late endosomes (B′–C′; GFP:Rab7; green) with *mtm* RNAi are shown. (D′–G′) Both *mtm* RNAi and null alleles resulted in enlarged acidified endolysosomes (LysoTracker, red; GFP-LAMP, green) that reverted to normal size with *mtm:GFP* cDNA (G). (H) Area of individual Rab5, GFP:Rab7, and LysoTracker-stained organelles in $Kc_{167}$ cells. (I–J′) Area of LysoTracker-positive organelles decreased in *mCherry:mtm*-expressing hemocytes. (K and K′) Ultrastructure of *mtm* RNAi $Kc_{167}$ cells revealed an increase in secondary lysosomes (shaded pink) and electron-lucent membrane compartments (arrowheads). (L and L′) Examples of secondary lysosomes. (M) Secondary lysosome area shown as the percentage of cell area (means: control, 1.8%; *mtm* RNAi cell area, 5.0%). (N–O′) Examples of electron-lucent membrane structures. Single membrane bound (N and N′) and double membrane bound, typical of autophagosomes (O and O′). (P) Number of individual electron-lucent compartments (means: WT, 1.4; *mtm* RNAi cell, 6.8). Proportion of single (75 and 78%) and double (25 and 22%) membrane-bound electron-lucent structures remained unaffected. Error bars indicate SEM.

Simonsen and Tooze, 2009). The ultrastructure confirmed formation of intraluminal vesicles of multivesicular bodies (unpublished data). These combined results indicate that *mtm* function affects endolysosomal homeostasis and is both necessary and sufficient to restrict endolysosomal size.

### Endocytosis contributes to separable *mtm* effects on endolysosomes and cell remodeling

Endolysosome homeostasis reflects a balance between membrane influx and efflux. We performed kinetic assays to test an *mtm* impact on trafficking to endolysosomes. The *mtm*-depleted cells exhibited normal early steps in phagocytosis, fluid phase, and cargo-mediated endocytosis. *Escherichia coli*, F-dextran, or BSA colocalization with the enlarged LysoTracker-positive compartments indicated successful traffic to endolysosomes (Fig. 5 A′; and Fig. S3, A and B), although the late steps of F-dextran delivery were delayed (Fig. 5 A′). To address the balance of specific membrane influx at late endosomes, we tested whether codepletion of *mtm* and effectors of endocytic or autophagic trafficking could suppress the enlarged endolysosomes (Fig. 5 B; and Fig. S3, C and D). Codepletion of *mtm* with either *Atg1*, a kinase involved in initiation of autophagy (Scott et al., 2004; Xie and Klionsky, 2007), or the endosomal GTPases *Rab5* or *Rab7* each restored or further decreased the size of LysoTracker organelles (Fig. 5, B and C). These results indicate that autophagic and endocytic routes contribute to the *mtm* endolysosomal defect and suggest that Mtm may negatively regulate influx of both routes either independently or at a single site of membrane convergence.

The two distinct defects in cortical remodeling and endolysosomal homeostasis raised the question of whether both *mtm* roles are related either as primary and secondary consequences or through a shared *mtm* function. If related, suppressors of the *mtm*-dependent enlarged endolysosomes could also revert the lack of cell protrusions. The codepletion of *mtm* with *Atg1* modified the phenotype but did not rescue lack of protrusion formation in either $Kc_{167}$ cells or hemocytes (Fig. 5 E′). Instead, *Atg1* single- and double-mutant cells exhibited novel mutant phenotypes with failure of cell elongation or spreading (Fig. 5, E and E′), respectively. This suggests an *mtm* role antagonistic to autophagy that mediates endolysosomal homeostasis separable or downstream from protrusion formation and signifies an additional role for autophagy in cellular remodeling (Kadandale et al., 2010). We found that although neither *Rab5* nor *Rab7* was required for the induced cell shape change, codepletion of either endosomal effector with *mtm* partially restored ecdysone-induced $Kc_{167}$ cellular elongation (Fig. 5 F). Together, these results suggest that endocytosis, but not endolysosomal size, impacts cortical remodeling and point to an *mtm* endocytic function with divergent effects on endolysosomal flux and cell protrusion formation.

Conversely, *mtm* may positively regulate the competing process of membrane efflux. *Rab11* RNAi on its own had little effect on endolysosomal size or $Kc_{167}$ cell elongation (Fig. 5, B, C, and F). This suggests that disrupted efflux of Rab11-recycling endosomes does not account for *mtm* mutant phenotypes without excluding a possible role for other membrane retrieval routes. Cell protrusions still formed upon knockdown of *Fab1* phosphoinositide kinase (Fig. 5 F and Fig. S3 E), which is shown to result in enlarged lysosomes (Fig. 5 C and Fig. S3 C) and disruption of $PI(3,5)P_2$ (Rusten et al., 2006), further dissociating endolysosomal size from cortical remodeling. In addition, *Fab1* coRNAi failed to rescue *mtm* RNAi phenotypes (Fig. 5, C and F), indicating that Mtm turnover of $PI(3,5)P_2$ alone also is unlikely to account for an *mtm* function in endolysosome homeostasis or cellular remodeling.

### Mtm down-regulates PI(3)P for endolysosomal membrane identity and dynamics

Common defects observed with null and catalytic mutant alleles suggest that *mtm* roles are phosphoinositide dependent (Figs. 2 and 3). As predicted, WT Mtm protein exhibited in vitro PI(3)P and $PI(3,5)P_2$ phosphatase activity, whereas the $Mtm^{R403C}$ form, mutated within the catalytic motif, was inactive (Fig. 6 A). If *mtm* function is mediated through its role in PI(3)P turnover, then *mtm* depletion or expression may alter PI(3)P accumulation. In WT $Kc_{167}$ cells and hemocytes, the GFP:2xFYVE PI(3)P biosensor (Gillooly et al., 2000; Wucherpfennig et al., 2003) localized primarily to puncta (Fig. 6 B) and rings (Fig. 6 C). Upon *mtm* depletion, we detected an expanded distribution of GFP:2xFYVE both on more numerous puncta and on enlarged rings (Fig. 6, B′ and C′). In contrast, overexpression of WT *mtm* cDNA disrupted GFP:2xFYVE localization to a diffuse cytoplasmic pattern (Fig. S4 D). Although GFP:2xFYVE showed extensive Rab5 colocalization and minimal overlap with LysoTracker-positive compartments in WT cells (Fig. 6 C, and not shown), GFP:2xFYVE surrounded large LysoTracker-positive organelles in *mtm*-depleted hemocytes (Fig. 6 C′), indicating a shift in the site of highest PI(3)P detected by the biosensor from early endosomes to endolysosomes.

Endosomal PI(3)P recruits effectors that promote membrane transport, tethering, and fusion (Lindmo and Stenmark, 2006). We observed extensive dispersion of GFP:2xFYVE upon *Rab5* but not *Rab7* RNAi (Fig. S4, A and A'), suggesting that genetic interactions between *mtm* and *Rab5* may be at the level of PI(3)P modulation, whereas interactions with *Rab7* may be at the level of PI(3)P effectors. Consistent with contribution of inappropriate or excessive membrane-tethering fusion, endolysosomal size was reverted with codepletion of *mtm* and genes encoding machinery of the HOPS complex or SNAREs (Fig. S3, C and D; Banta et al., 1988; Seals et al., 2000; Jahn et al., 2003).

PI(3)P-containing compartments in WT cells exhibited highly dynamic behavior with directional movement (Fig. 6 D) and tubulation indicative of exiting membrane (Fig. 6 E and Video 2). In contrast, *mtm*-depleted cells lacked motile PI(3)P-containing particles. Instead, 2xFYVE was detected on rings with restricted, conjoined motion and little obvious tubulation (Fig. 6, D′–E′; and Video 2), which is consistent with inappropriate PI(3)P accumulation disrupting membrane efflux and promoting excessive tethering and fusion between compartments (Fig. 6 E′). Reflecting the PI(3)P membrane dynamics in

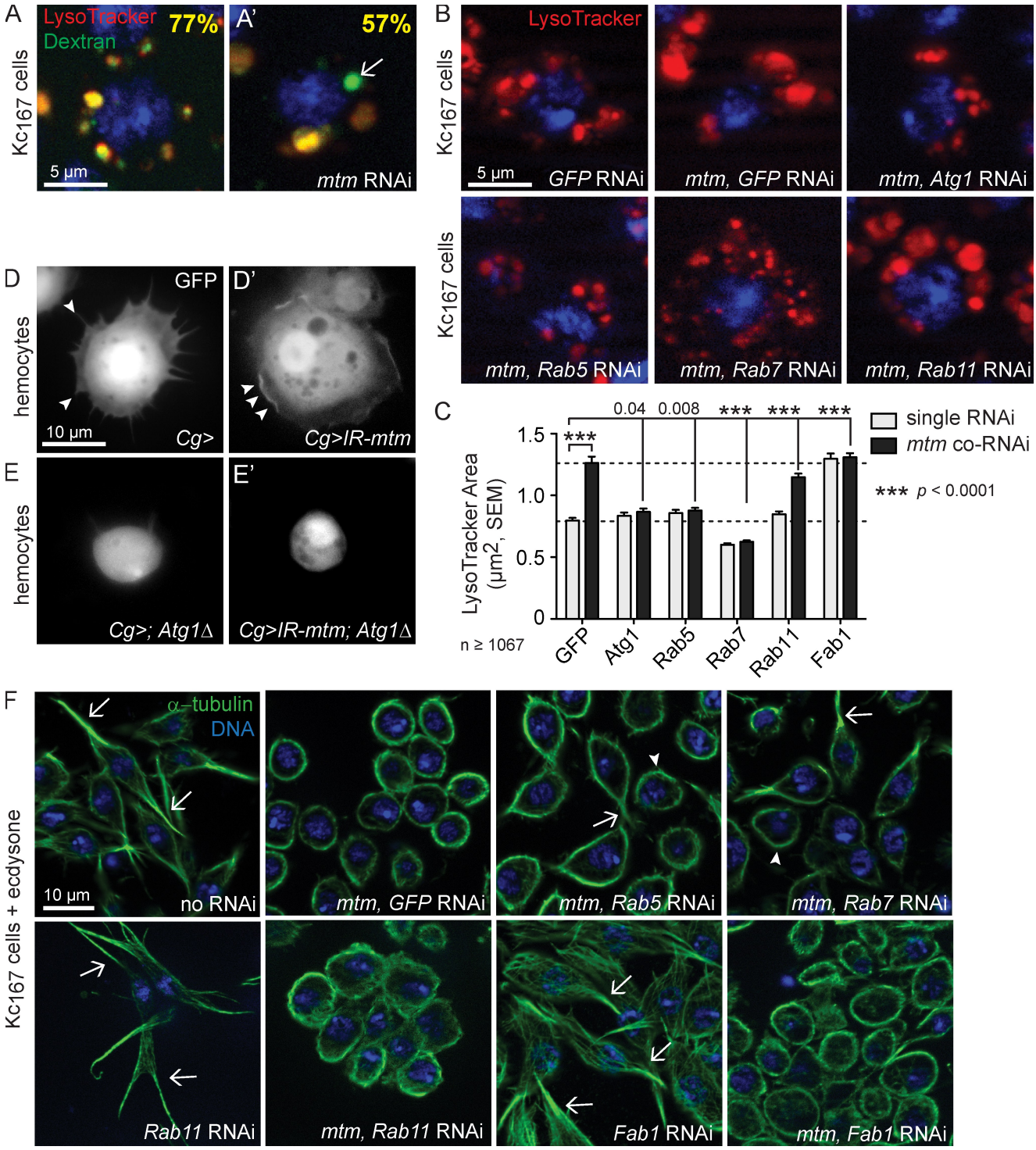


Figure 5. ***mtm* interacts with both endocytic and autophagic effectors, with separable effects on endolysosomes and cell remodeling.** (A and A') Arrow indicates delay in late F-dextran (green) trafficking to LysoTracker-positive organelles (red) in *mtm* RNAi $Kc_{167}$ cells, shown as the percent of colocalization 20 min after uptake. (B and C) Screen of endolysosome size in single and *mtm* coRNAi–treated $Kc_{167}$ cells, identified suppressors of *mtm*-enlarged endolysosomes. (B) LysoTracker (red) with coRNAi as shown. (C) Quantification of mean endolysosomal area upon single RNAi (gray) or *mtm* coRNAi (black). Bottom dashed line, mean area *GFP* RNAi; top dashed line, mean area of *mtm, GFP* coRNAi. (D) GFP-labeled $Atg1^{\Delta 3D}/+$ hemocytes with extended protrusions (arrowheads). (D') Lack of cell protrusions (ruffles, arrowheads) in spread *mtm*-depleted hemocytes. (E) Round $Atg1^{\Delta 3D-/-}$ hemocytes failed to spread. (E') Round cells with $Atg1^{\Delta 3D-/-}$ in combination with *mtm* depletion. (F) Microtubules (green) in $Kc_{167}$ cells 1 d after ecdysone with coRNAi as shown. With *mtm* and *Rab5* or *Rab7* codepletion, mixed examples of cells that partially reverted cell extensions (arrows) and cells that remained round (arrowheads). No effect of *Rab11* or *Fab1* RNAi alone or on *mtm* RNAi defect. Error bars indicate SEM.

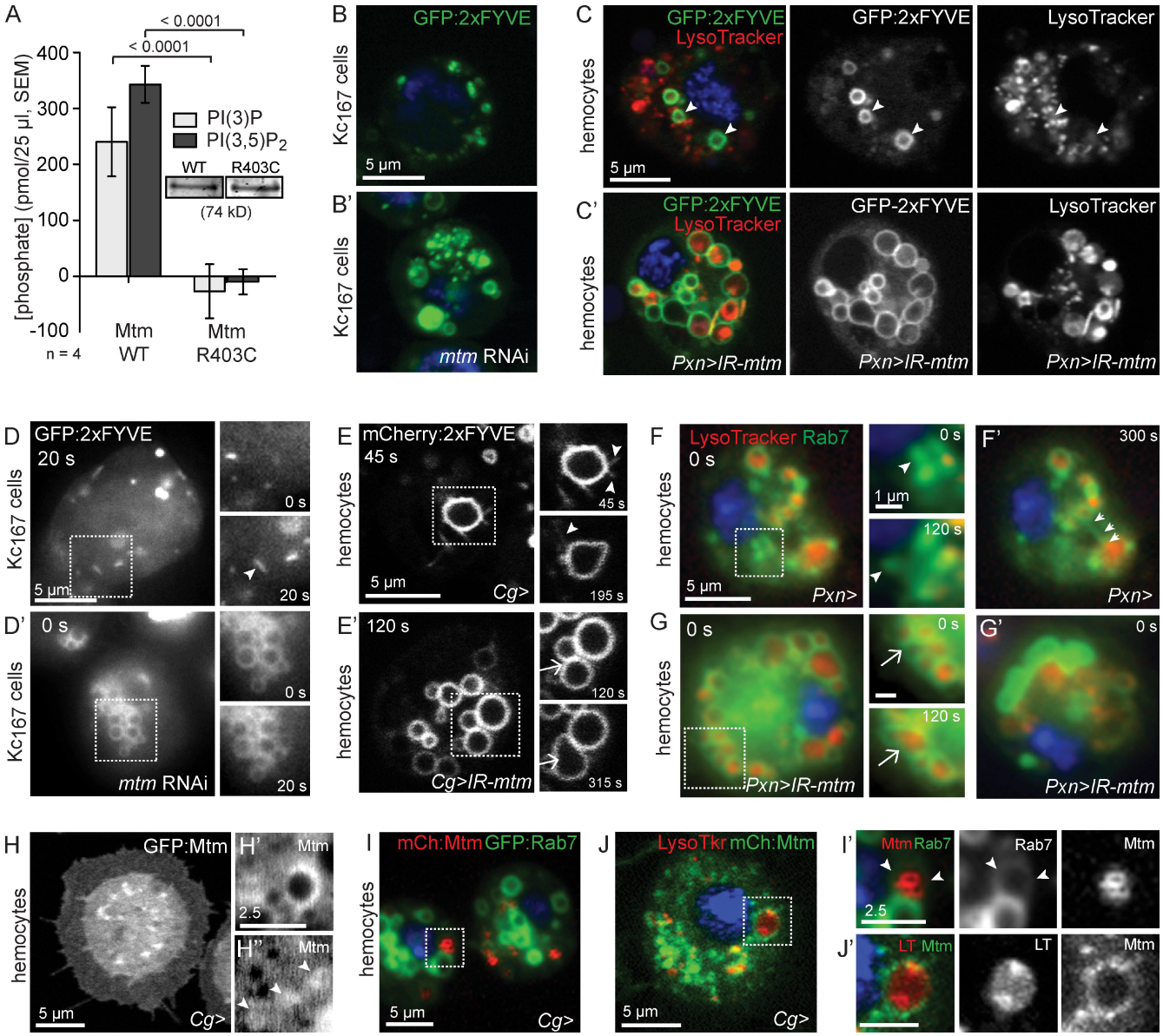


Figure 6. ***mtm* controls PI(3)P turnover, membrane compartment identity, and flux.** (A) Mtm-dephosphorylated PI(3)P and PI(3,5)$P_2$. Mutant Mtm-R403C was inactive for both substrates (released phosphate/reaction). (B–E′) PI(3)P distribution detected by GFP:2xFYVE. PI(3)P expanded distribution upon *mtm* RNAi in $Kc_{167}$ cells (B′) and abnormal association with LysoTracker-positive organelles upon *mtm* depletion in hemocytes (C′). (D) PI(3)P pools detected within small dots with rapid, directional movement (arrowhead; motile particle imaged as line) by time-lapse microscopy in control $Kc_{167}$ cells. (D′) PI(3)P pools detected on expanded, tethered rings and lack of particle motility upon *mtm* RNAi. (E) Time-lapse microscopy of PI(3)P pools detected by mCherry:2xFYVE on rings with obvious tubulation (arrowheads) in hemocytes. (E′) PI(3)P pools detected on expanded, tethered rings that underwent fusion (arrows) without detectable tubulation in *mtm*-depleted hemocytes; still images from Video 2 are shown. (F and F′) GFP:Rab7 motility (F, arrowheads) and dynamic extension and retraction of tubules (F′, arrows) in control hemocytes (Video 3). LysoTracker, red; DAPI, blue. (G and G′) Tethered motion and fusion (arrows) between enlarged GFP:Rab7 compartments in *mtm*-depleted hemocytes. (H–H″) GFP:Mtm localized to dots (H) and big (H′) and small rings (H″, arrowheads). (I and I′) mCherry:Mtm on small rings detected within GFP:Rab7 compartments (GFP:Rab7 ring, arrowheads). (J and J′) Mtm at periphery of acidified endolysosomes. Red, LysoTracker. Boxed areas are shown in higher magnification on the right. Error bars indicate SEM.

WT hemocytes, we similarly observed motile GFP:Rab7- or LysoTracker-positive particles (Fig. 6 F) and dynamic GFP:Rab7 tubules suggestive of efflux from endolysosomes (Fig. 6 F′ and Video 3). In contrast, *mtm*-depleted cells contained adjacent LysoTracker-positive GFP:Rab7 rings that exhibited localized movements and infrequent tubulation (Fig. 6, G and G′; and Video 3). In both WT and *mtm*-depleted conditions, we observed GFP:Rab7 fusion events (Fig. 6 G). These results suggest that Mtm is important, perhaps through or in addition to a role in promoting efflux, to down-regulate PI(3)P-mediated tethering and fusion of Rab7-containing late endosomes.

### Mtm associates with internal membranes, including endolysosomes

Given its multiple cellular functions, we asked where Mtm protein localized. When expressed as different tagged forms, Mtm was diffuse throughout the cell and localized to puncta and rings (Fig. 6, H–H″), including faint, small rings of uniform size

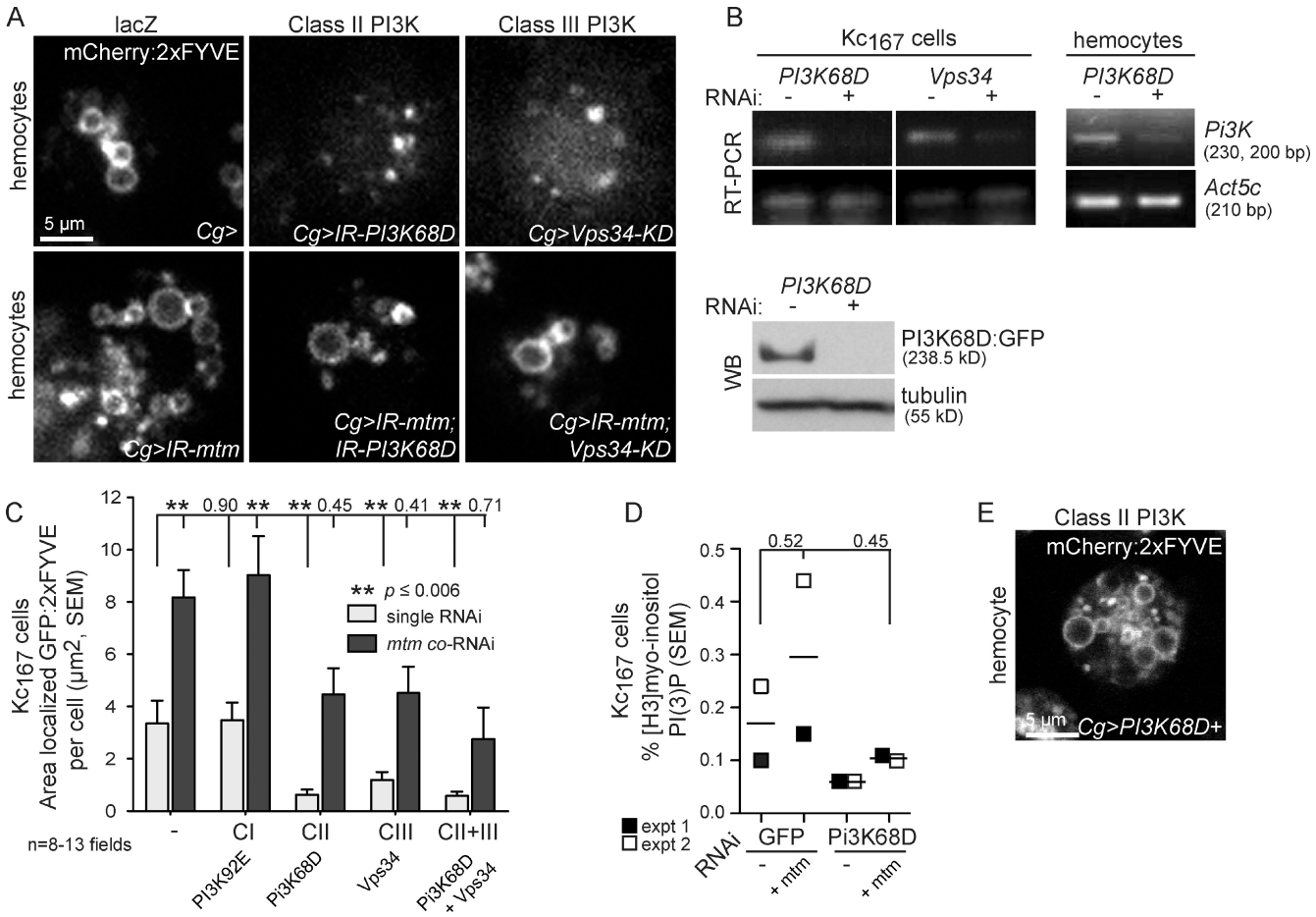


Figure 7. ***mtm* interacts with both class II *Pi3K68D* and class III *Vps34* for PI(3)P homeostasis.** (A) PI(3)P distribution, as detected by mCherry:2xFYVE in single hemocyte for genotypes as shown, was expanded (*IR-mtm*), depleted (*IR-Pi3K68D* or *Vps34-KD*), or restored (bottom; *IRmtm* with *IR-Pi3K68D* or *Vps34-KD*). (B) Depletion of *Pi3K68D* or *Vps34* transcripts in RNAi-treated $Kc_{167}$ cells (left) and purified hemocytes (right; *Pxn-GAL4/UAS-IR-Pi3K68D*). Pi3K68D:GFP (bottom; anti-GFP) in RNAi-treated $Kc_{167}$ cells. WB, Western blot. (C) GFP:2xFYVE area in RNAi-treated $Kc_{167}$ cells (Fig. S4 C) normalized per cell number. Single-kinase RNAi (gray) or *mtm* coRNAi (black). (D) Percent PI(3)P of total *myo*-inositol from RNAi-treated $Kc_{167}$ cells. Similar trends were found across two experiments. (E) *Pi3K68D:GFP* expression expanded PI(3)P detected by mCherry:2xFYVE. Error bars indicate SEM.

(Fig. 6 H″, arrowheads), which are indicative of membrane structures. Mtm did not colocalize with Rab5 or GFP:Rab7 endosomes. However, small rings of mCherry:Mtm could be found inside a subset of GFP:Rab7 compartments (Fig. 6, I and I′), which is suggestive of intraluminal vesicles or autophagosomes (Xie and Klionsky, 2007). A small fraction of Mtm was detected at acidified compartments as puncta or completely surrounding LysoTracker-positive organelles (Fig. 6, J and J′), which is consistent with roles in endolysosomal homeostasis.

### Both class II and class III PI(3)-kinases contribute to PI(3)P pool antagonized by *mtm*

If Mtm dephosphorylates a distinct PI(3)P pool, *mtm* function could antagonize the PI(3)P production by a specific PI3-kinase. As in mammals, *Drosophila* encodes three classes of PI3-kinases, with one member per class capable of PI(3)P synthesis in vitro (class I, *Pi3K92E*; class II, *Pi3K68D*; and class III, *Vps34*). Vps34 was a likely candidate for production of an Mtm-functional substrate given known roles for PI(3)P synthesis on early endosomes and for autophagy (Lindmo and Stenmark, 2006). In testing all three PI3-kinases, we found that knockdown or expression of kinase-dead form of *Vps34* and, surprisingly to an even greater extent, knockdown of *Pi3K68D* each individually resulted in dispersion of localized 2xFYVE biosensors (Fig. 7, A–C; and Fig. S4, B and C), demonstrating that both class II and III PI3-kinases are required for significant PI(3)P pools in immune cells. A recovery of the 2xFYVE-localized distribution was obtained from codisruption of *mtm* with *Pi3K68D* or *Vps34* (Fig. 7, A and C; and Fig. S4 C), indicating that interference with either PI3-kinase was sufficient to restore the *mtm*-dependent PI(3)P imbalance. Given that Pi3K68D contribution to PI(3)P synthesis has not been characterized in vivo, we further investigated its role directly. We confirmed the effects on PI(3)P total cellular levels from *myo*-inositol radiolabeled $Kc_{167}$ cell lysates (Fig. 7 D). Altered levels of PI(3)P were observed upon knockdown of *mtm* phosphatase (1.7-fold increase) and *Pi3K68D* kinase (2.8-fold decrease), respectively, that returned nearer to normal levels upon their codepletion (1.6-fold decrease; Fig. 7 D), mirroring the genetic interaction seen with 2xFYVE distribution. Overexpression of *Pi3K68D* cDNA phenocopied *mtm* depletion effects of expanded 2xFYVE

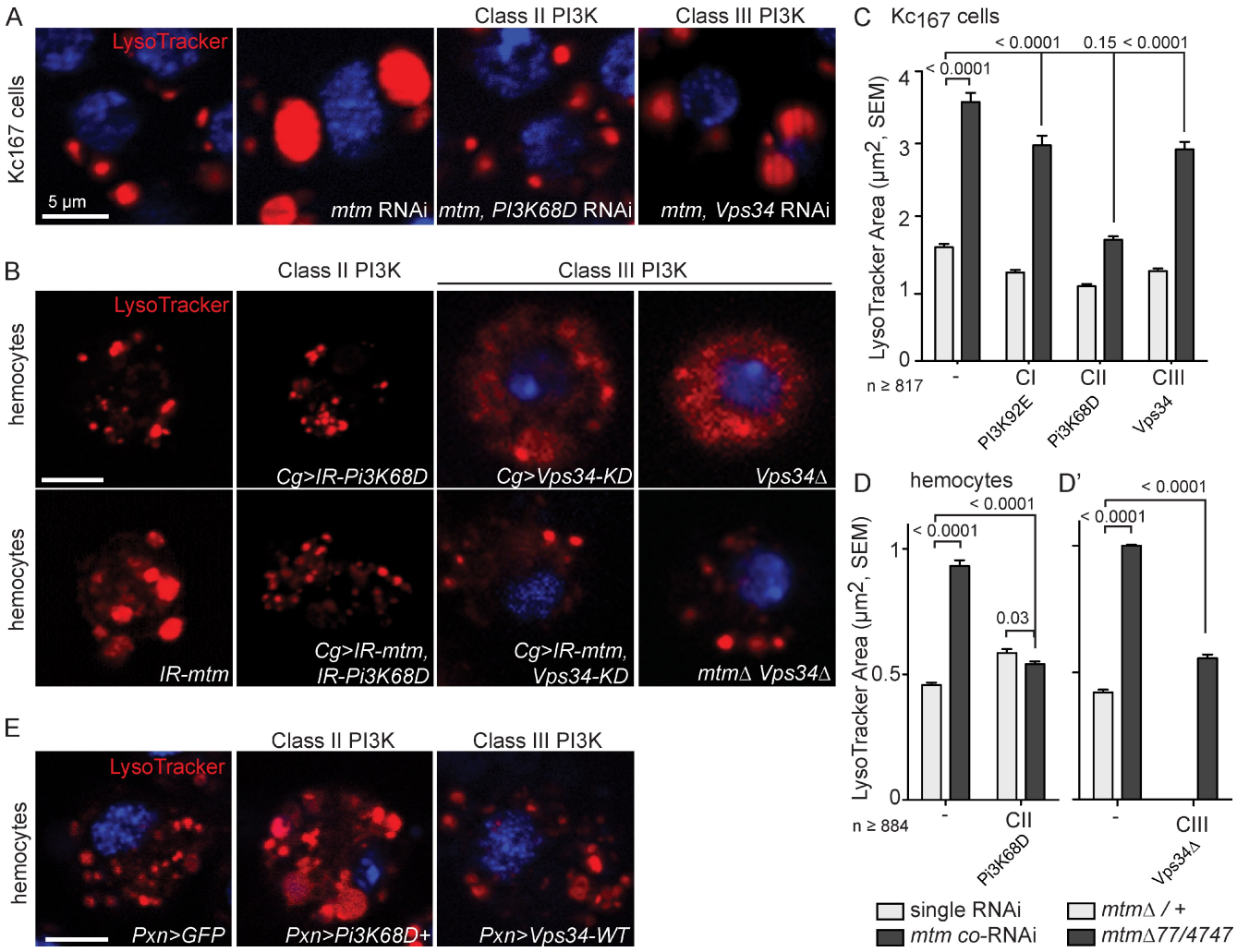


Figure 8. ***mtm* and class II *Pi3K68D* have opposing roles for endolysosome homeostasis, distinct from class III *Vps34*.** LysoTracker, red; DAPI, blue; shown for single cell. (A) Rescue of endolysosomal size upon *mtm, Pi3K68D* coRNAi in $Kc_{167}$ cells. (B, bottom) In hemocytes, class II PI3K depletion (*IRPi3K68D*) rescued *mtm*-dependent endolysosome size. Class III PI3K disruption alone (*Vps34-KD,* kinase dead, or $vps34^{\Delta m22}$) resulted in diffuse LysoTracker staining (top) rescued by *mtm* disruption. (C–D′) Size of individual LysoTracker-positive organelles upon single RNAi (gray) and *mtm* coRNAi (black) in $Kc_{167}$ cells or hemocytes (D and D′; $Vps34^{\Delta}$ unquantifiable). (E) *Pi3K68D:GFP* expression (*Pxn-GAL4*) led to enlarged endolysosomes, whereas *Vps34-WT* had little effect. Error bars indicate SEM.

distribution (Fig. 7 E and Fig. S4 E), which is consistent with Pi3K68D synthesis of PI(3)P.

### Class II Pi3K68D and *mtm* have opposing functions for homeostasis of endolysosome size

If Mtm roles are mediated through down-regulation of a distinct PI(3)P pool, then *mtm* could antagonize the function of a specific PI3-kinase. As observed for PI(3)P, codepletion of *Pi3K68D* with *mtm* suppressed the giant endolysosome size (Fig. 8, A–D). Conversely, we found that overexpression of *Pi3K68D* cDNA in WT hemocytes resulted in greatly enlarged LysoTracker-positive organelles (Fig. 8 E). This condition phenocopyied *mtm* depletion and is consistent with Pi3K68D coregulation of a PI(3)P pool important for endolysosomal size. Although both *Vps34* and *Pi3K68D* disruption reduced 2xFYVE-detected PI(3)P distribution to a similar degree (Fig. 7, A and C), knockdown of *Vps34* alone or in combination with *mtm* exhibited minor effects on LysoTracker-positive organelles in $Kc_{167}$ cells (Fig. 8, A and C). Disruption of *Vps34* with either a null mutant allele or targeted expression of a kinase-dead form in hemocytes, however, resulted in diffuse LysoTracker staining throughout the cells (Fig. 8 B), suggesting disruption of lysosomal $H^+$-ATPase trafficking or of the integrity or size of acidified organelles. Codepletion or double mutants of *Vps34* and *mtm* suppressed both individual endolysosomal defects in hemocytes. Unlike *Pi3K68D*, overexpression of *Vps34* WT cDNA in hemocytes had little to no effect on LysoTracker-positive organelles (Fig. 8 E). These results suggest that *mtm* is antagonistic to both *Pi3K68D* and *Vps34* functions but that each kinase exhibits distinct roles for normal acidified endolysosomes and differential requirements in $Kc_{167}$ cells and hemocytes.

### Pi3K68D localizes at endolysosomes and cortex with microtubule-dependent motility

Similar to Mtm, multiple tagged forms of Pi3K68D protein localized to internal puncta and rings (Fig. 9, A and A′) and

failed to colocalize with Rab5 or GFP:Rab7 but partially associated with acidified organelles (Fig. 9, B and B′). Mtm and Pi3K68D did not colocalize nor obviously deviate in their patterns when coexpressed (Fig. 9 C), suggesting either non- or only transiently overlapping domains. Strikingly, Pi3K68D also aligned along the hemocyte periphery (Fig. 9 A). The cortical Pi3K68D often appeared filamentous (Fig. 9 A″, arrows) and colocalized with microtubules (Fig. 9, D and D′) independent of F-actin (Fig. 9, E–F). The distinct localization patterns raised the questions of how Mtm and Pi3K68D might coregulate a common PI(3)P pool and whether Pi3K68D localization was dynamic. Time-lapse microscopy revealed Pi3K68D:GFP oscillations (Fig. 9 G) and directed motility as small particles, including movement to and away from LysoTracker-positive organelles (Fig. 9 J and Video 4). Pi3K68D motility was coincident (Fig. 9 H) and dependent on microtubules (Fig. 9 I), which is consistent with known mechanisms of vesicular transport and endosomal dynamics (Soldati and Schliwa, 2006). Thus, conserved class II Pi3K microtubule-dependent dynamics (PI3KC2α; Zhao et al., 2007) may mediate Pi3K68D roles at cortical and internal sites.

### Class II Pi3K68D loss of function suppresses *mtm* requirement for cortical remodeling

The *mtm* roles for endolysosomes and in cortical remodeling could be related to regulation of a single PI(3)P pool or independent regulation of different spatial pools or PIP forms. Neither disruption nor overexpression of either *Pi3K68D* or *Vps34* alone had a noticeable effect on hemocyte spreading or F-actin protrusions (Fig. S4, F and G). We found that *Pi3K68D* strongly suppressed the *mtm* RNAi block in $Kc_{167}$ cell elongation (Fig. 10 A) and completely rescued hemocyte protrusion formation (Fig. 10 B). In contrast, *Vps34* knockdown partially modified *mtm* RNAi inhibition of $Kc_{167}$ cell elongation (Fig. 10 A) and showed infrequent and only mild modification of hemocyte protrusions in *mtm* double-mutant combinations (Fig. 10 B). Importantly, the effect of *mtm* RNAi on abnormally clumped hemocyte distribution in larvae was also reverted by *Pi3K68D* codepletion (Fig. 10 C). These results point to a functional interaction between *Pi3K68D* and *mtm* that modulates cortical dynamics and suggests that their direct coregulation of a distinct PI(3)P pool plays an important role in the balance of hemocyte protrusion formation and distribution in vivo.

### Mtm and class II Pi3K68D collaborate broadly for animal viability

Unlike *mtm*, class II or III PI3-kinase functions in hemocytes were not required for animal viability. However, animal lethality resulted from *Pi3K68D* cDNA expression in tissues that also exhibited essential *mtm* functions (Cg-GAL4 and DMef2-GAL4; Table S1), consistent with overproduction of an Mtm PI(3)P substrate pool. Furthermore, *Pi3K68D* and *mtm* codisruption in other tissues, including in muscle, fully rescued (GAL4 drivers 24B, DMef2, 69B, and Ptc) or suppressed (GAL4 drivers Act5c, Cg, and Pxn) viability or visible phenotypes (Table S1). This indicates disruption of class II PI3-kinase as a potent and broad suppressor of *mtm*-dependent functions in vivo.

## Discussion

We identified a class II Pi3K68D-dependent PI(3)P pool as a functional and likely direct Mtm substrate. We demonstrated that *Pi3K68D* and *mtm* played major roles in the coregulation of a hemocyte PI(3)P pool and that both were necessary and sufficient for PI(3)P-mediated endolysosomal homeostasis. Alternatively, *mtm* and *Pi3K68D* could interact through interconverted PIP pools, e.g., if class II PI3K synthesis of $PI(3,4)P_2$ (MacDougall et al., 1995) led to inositol polyphosphate 4-phosphatase generation of endosomal PI(3)P (Norris and Majerus, 1994).

Importantly, *Pi3K68D* loss of function suppressed multiple *mtm*-dependent hemocyte functions and essential roles in multiple tissues. Our results suggest that a conserved pathway linking MTM1/MTMR2 and class II PI3-kinases could also be important for similar roles in mammals. Expression of human *MTMR2* in flies rescued the lethality associated with *mtm* depletion in different tissues, highlighting potential significance from use of the fly to better understand *MTMR2*-related human disease. Recent studies in T cells identified roles for PI3KC2α and MTMR6 in PI(3)P-mediated regulation of a calcium-activated $K^+$ channel (Srivastava et al., 2005, 2009), indicating that class II PI3-kinases may play broad and dedicated roles in conjunction with different MTM family members.

We found that a subset of *mtm* functions also shared interactions with class III PI3-kinase, *Vps34*. The genetic interactions observed between *mtm* and *Vps34* in PI(3)P and endolysosomal homeostasis, but not cell remodeling or essential functions in different tissues, suggest several possibilities. *Vps34* function may regulate a *Pi3K68D* function or be partially redundant with *Pi3K68D* for certain *mtm* functions; *Vps34* may indirectly interact with *mtm* through converging PI(3)P membrane pools, and/or there may be additional essential consequences of *Vps34* functions, e.g., that antagonize different MTM family member functions. Similar partial and redundant interactions have been observed in *Caenorhabditis elegans*, where reduction of *mtm-1* rescued endocytosis defects but not lethality of *vps-34* mutants (Xue et al., 2003), and increased apoptotic cell corpse engulfment upon *mtm-1* depletion was found dependent on both *vps-34* and the class II *PIKI-1* functions (Zou et al., 2009).

We found that *mtm* was not only required for but could also promote cortical remodeling, specifically modulating cell protrusion formation. MTMs have not previously been ascribed specific roles in cellular remodeling, although MTM1/MTMR2 and PI3KC2 isoforms have been associated with the cortex, and MTM1 overexpression led to cell protrusions (Kim et al., 2002). Cortical F-actin organization and dynamics are under control of competing Rho GTPase activities, namely roles for Rac, Rho, and Cdc42 in lamellipodia versus protrusion formation (Ridley, 2006). A mutant form of MTM1 was detected at the plasma membrane upon constitutive Rac1 GTPase activation (Laporte et al., 2002), *mtm-1* was identified as a negative regulator of Rac-mediated engulfment (Zou et al., 2009), and Rho1 pathway hyperactivation resulted from combined essential function of *ymr1* (MTM), *sjl2*, and *sjl3* lipid phosphatases in yeast PI(3)P regulation (Parrish et al., 2005). However, PI3KC2β-expressing cell lysates exhibited increased levels of activated Cdc42 (Domin

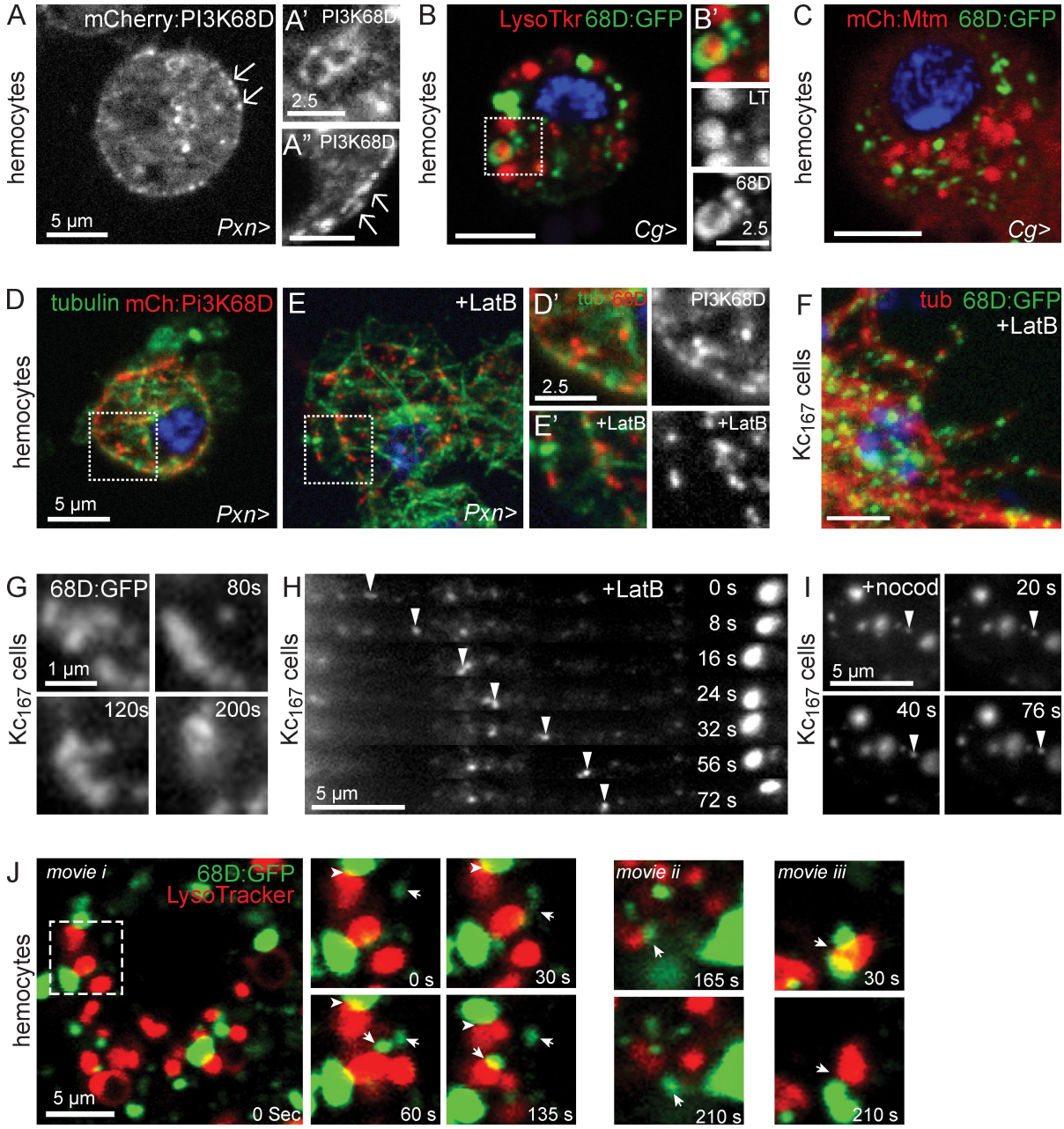


Figure 9. **Pi3K68D localizes at endolysosomes and cell periphery with microtubule-dependent motility.** (A–A") mCherry:Pi3K68D localized to dots (A and A'), rings (A and A"), and cell periphery (arrows) in hemocytes. (B and B') Pi3K68D:GFP surrounding acidified endolysosomes. Red, LysoTracker. (C) Mtm (red) and Pi3K68D (green) did not colocalize when coexpressed. (D–I) Pi3K68D microtubule-dependent motility and localization. (D and D') mCherry: Pi3K68D (red) along microtubules (green). (E and E') Localization persisted with latrunculin B (+LatB). (F) Pi3K68D:GFP colocalized with microtubules (red) in latrunculin B–treated $Kc_{167}$ cells. (G–I) Pi3K68D:GFP time-lapse imaging in live $Kc_{167}$ cells. (G) Pi3K68D on oscillating puncta. (H) Disruption of F-actin (+LatB) revealed extensive Pi3K68D:GFP particle motility (arrowheads). (I) Disruption of microtubules (+nocod) arrested all Pi3K68D:GFP motility. Arrowheads, examples of stationary Pi3K68D:GFP particles. (J) Pi3K68D:GFP dynamic colocalization relating to LysoTracker (red) compartments in single z sections from time-lapse microscopy of hemocytes (the following show frames from Video 4: PI3K68D:GFP movement toward [i] and away [ii and iii] from endolysosomes). Examples of persistent (arrowheads) and transient colocalization between motile Pi3K68D:GFP (arrows) and Lysotracker. Blue, DAPI. Boxed areas are shown in higher magnification on the right.

et al., 2005), and PI3KC2α depletion interfered with Rho-mediated smooth muscle contraction (Yoshioka et al., 2007). Interestingly, endocytic trafficking of Rac was shown important for its spatially regulated activity (Palamidessi et al., 2008). Thus, one consequence of opposing *Pi3K68D/mtm* functions in hemocytes may be in the cortical balance of specific Rho GTPases, either through PI(3)P-mediated membrane trafficking or recruitment of PI(3)P-binding regulatory proteins to discrete membrane domains.

Our experiments show that Mtm has a role in policing traffic at the late endosome, which is consistent with a normal function to down-regulate membrane influx and promote efflux. *mtm* was important to maintain the balance, but not ability, for membrane influx from endocytic and autophagic routes.

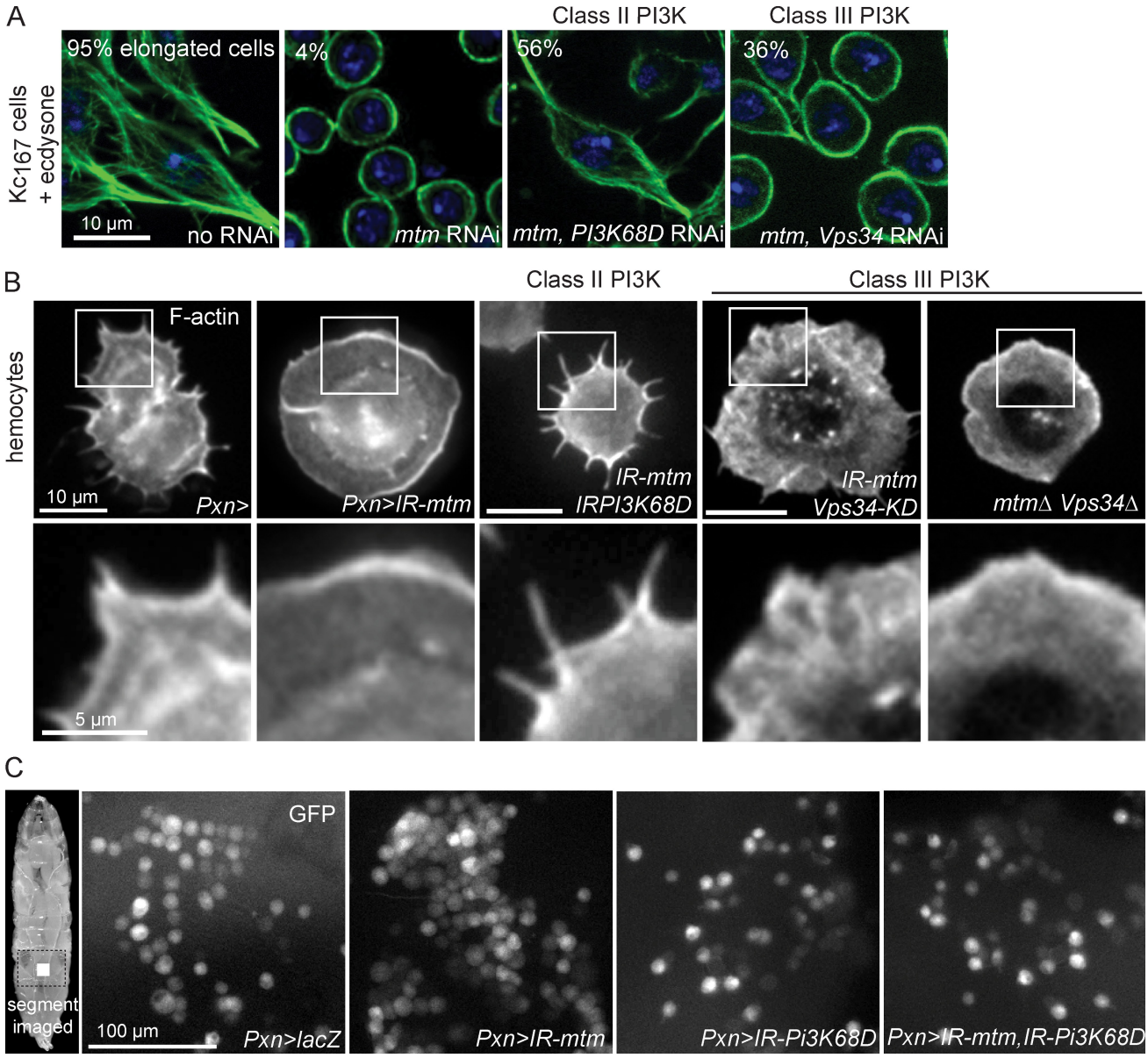


Figure 10. ***mtm* and class II *Pi3K68D* interact for normal hemocyte protrusions and distribution.** (A) Microtubules (green) are shown. 95% $Kc_{167}$ cells elongated 1 d after ecdysone. *mtm* RNAi blocked elongation (4%) and was reverted upon *Pi3K68D* coRNAi (56%) and less so by *Vps34* coRNAi (36%). (B) F-actin in hemocytes (top) and zoom of cell edges (bottom). *Pi3K68D, mtm* coknockdown rescued lack of hemocyte protrusions (*UAS-IRPi3K68D*$^{16240}$, *UAS-IRmtm*$^{3.5}$*/Pxn-GAL4*). Weakly modified or persistent lack of protrusions with coexpression of *mtm* RNAi and *Vps34-KD* (*UAS-Vps34-KD*$^{m8}$, *UAS-IRmtm*$^{3.1}$*/+; Pxn-GAL4/+*) or in double mutants (*mtm*$^{\Delta 77}$, *Vps34*$^{\Delta m22}$*/mtm*$^{z2\text{-}4747}$, *Vps34*$^{\Delta m22}$). (C) GFP-positive hemocytes (Pxn-GAL4) in intact larvae. *mtm* and *Pi3K68D* coRNAi reverted clumped to normal hemocyte distribution. Boxed areas are shown in higher magnification on the bottom.

We found through genetic interactions, marker analysis, and time-lapse microscopy that *mtm* function antagonizes PI(3)P-mediated membrane flux consistent with known roles in transport, tethering, and fusion of endosomes with lysosomes and of autophagosomes with late endosomes (Simonsen and Tooze, 2009). Importantly, *mtm*-dependent functions for endolysosomal size and cortical remodeling were separable, as indicated by *mtm* interactions with *Atg1* or *Vps34* that rescued endolysosome size but not hemocyte protrusions. Live cell imaging also revealed lack of dynamic tubulation, indicative of exiting membrane, in *mtm*-depleted hemocytes, suggesting that *mtm* function promotes undetermined routes of membrane efflux from PI(3)P-containing compartments. In addition, several results point to a role for *mtm* in autophagy: the increased number of double-membrane–bound structures and autophagolysosomes in *mtm*-depleted cells, reversion of enlarged endolysosomal size with *mtm* and *Atg1* codepletion, and Mtm localization to small rings associated with LysoTracker-positive organelles and within Rab7 compartments, suggestive of autophagosomes. Given the PI(3)P dependence and intersection with endolysosomes, there are likely roles for MTM phosphatase regulation in autophagy (Vergne et al., 2009).

Collectively, we favor a model that a PI(3)P pool directly coregulated by Pi3K68D-mediated synthesis and Mtm-mediated turnover is involved in membrane delivery and exit, respectively, at an endosomal compartment that maintains homeostasis of both

cortical dynamics and endolysosome size. Pi3K68D localization and motility suggest interaction at the level of dynamic PI(3)P pools synthesized at the cortex or on internal membranes. The lack of cell protrusions upon *mtm* disruption could result from elevated Pi3K68D-dependent PI(3)P that inhibits membrane efflux to undefined recycling endosomes and, thus, blocks redelivery of a cortical regulator that promotes cell protrusions. *Pi3K68D* overexpression did not phenocopy the lack of protrusions, which may indicate that Pi3K68D requires a limiting cofactor or scaffold protein or that levels of Mtm are sufficient to override ectopic activity. Conversely, ectopic cell protrusions that form upon Mtm overexpression could result from inappropriate depletion of a Pi3K68D-synthesized PI(3)P pool that leads to excessive efflux, and, thus, persistent recycling of the same cortical regulator. Consistent with this, an endosomal-tethered form of MTM1 was able to induce membrane tubulation (Fili et al., 2006). In turn, *mtm* function down-regulates PI(3)P-mediated endosome transport, tethering, and fusion, restricting endolysosome size.

Our genetic analysis uncovered critical requirements for *mtm*- and phosphoinositide-dependent muscle and immune cell functions in *Drosophila*. Defects in remodeling cell shape upon either knockdown or overexpression of *mtm* both corresponded with defects in hemocyte dispersion and recruitment to wound sites. These results indicate the significance of *mtm*-dependent cellular regulation to immune cell behaviors in the animal, analogous to those performed by mammalian macrophages in response to wounding and infection. The identification of Pi3K68D-generated PI(3)P pools as a likely in vivo substrate of Mtm, and the specific cellular roles modulated by the balance of this pool in animals, has significance in better understanding roles for conserved MTM1/MTMR2 and PI3KC2 in mammals. Our results highlight the potential that class II PI3K-activating mutations could underlie unassigned MTM-related human diseases. Furthermore, class II PI3K could serve as a therapeutic target to oppose deleterious effects of MTM mutations associated with human disease.

## Materials and methods

### *Drosophila mtm* mutations and genetics

Excision alleles $mtm^{\Delta 77}$ and $mtm^{\Delta 210}$ were isolated after Δ2-3 mobilization of viable P(EPgy2)CG9117 for lethality over Df(2L)ED338 and molecularly determined by sequencing of genomic DNA amplicons spanning the excisions from homozygous mutant larvae. Point mutation allele $mtm^{z2\text{-}4747}$ was identified with help from the Fly-TILL service (Cooper et al., 2008). The *mtm* genomic alleles were balanced over *CyO, P{w[+mC]=ActGFP}JMR1*, and presence or absence of GFP was used for determination of lethal phase and selection of homozygous and trans-heterozygous larvae raised at 25°C.

RNAi hairpin constructs made from 395- (201–202) or 565-bp (203–204) *mtm* genomic amplicons with primers (201F) 5′-GTACTCTAGATATTGACAACACACTGTGGCTAAA-3′, (202R) 5′-GTACTCTAGAAGTACAGATGATCCACGATGGTTA-3′, (203F) 5′-GTACTCTAGACTTACCATAACCAACTACCGTCTG-3′, and (204R) 5′-GTACTCTAGAACCTTGTAATGGTCGCTTGAGT-3′ were cloned with XbaI restriction sites into upstream activating sequence (UAS)–containing pWIZ vector sequentially at NheI and AvrII sites (Lee and Carthew, 2003), and orientation was confirmed by sequencing. Fly injections (Best Gene) generated viable transformant lines, including *UAS-IR:*$mtm^{3.1}$ (II) and *UAS-IR:*$mtm^{3.5}$ (III) with 201–202 fragment in "heads-in" orientation used in this study. When 2xIRmtm is noted, *UAS-IR:*$mtm^{3.1}$*; UAS-IR:*$mtm^{3.5}$ stock was used. Crosses using RNAi hairpins were raised at 29°C to maximize GAL4-driven expression.

Genotypes used in this study included (1) *w; UAS-GFP:Rab7/CyO* (Entchev et al., 2000) and *w; UAS-GFP:Rab7, UAS-IR*$mtm^{3.1}$*/CyO*, (2) *w; UAS-GFP:myc:2xFYVE/CyO* (Wucherpfennig et al., 2003) and *w; UAS-GFP:myc:2xFYVE, UAS-IR*$mtm^{3.1}$*/CyO*, (3) *w; UAS-mCherry:2XFYVE*$^2$, (4) *w; UAS-mtm:eGFP*$^7$ and *w; UAS-IR*$mtm^{3.1}$*; UAS-mtm:eGFP*$^7$, (5) *w; UAS-eGFP:MTMR2*$^5$ and *w; UAS-IR*$mtm^{3.1}$*, UAS-eGFP:MTMR2*$^5$, (6) *w; UAS-mCherry:mtm*$^7$ and *w; UAS-eGFP:mtm*$^4$, (7) *w[1118]; UAS-IRPi3K68D* transformant lines 16239 and 16240, and *w[1118]; UAS-IRFab1*$^{27591}$ (Dietzl et al., 2007) and *w; UAS-IRPi3K68D*$^{16240}$*, UAS-IR*$mtm^{3.5}$, (8) *w; UAS-mCherry:Pi3K68D*$^{2.1}$*/CyO, w; UAS-mCherry:Pi3K68D*$^{2.2}$*/TM6 Hu Tb* and *w; UAS-Pi3K68D:eGFP*, (9) *yw, hs-FLP; UAS-Vps34-KD*$^{m8}$ (Juhász et al., 2008) and *w; UAS-Vps34-KD*$^{m8}$*, UAS-IR*$mtm^{3.1}$, (10) *yw, hs-FLP; UAS-Vps34-WT*$^{m7}$ (Juhász et al., 2008), (11) *w;* $Vps34^{\Delta m22}$*/CyO-GFP-B* (Juhász et al., 2008), *w;* $mtm^{\Delta 77}$*,* $Vps34^{\Delta m22}$*/CyO,ActGFP*, and *w;* $mtm^{z2\text{-}4747}$*,* $Vps34^{\Delta m22}$*/CyO,ActGFP*, (12) *w[1118];* $P\{w[+mC]=Cg\text{-}GAL4.A\}^2$ (Asha et al., 2003), (13) *w; Cg-GAL4,* $P\{w[+mC]=UAS\text{-}2xEGFP\}^{AH2}$, (14) *w; Cg-GAL4, UAS-mCherry:myc:2xFYVE*$^2$, (15) *w; Cg-GAL4, UAS-mCherry:mtm*$^7$, (16) *w;* $Pxn\text{-}GAL4^{8.1.1}$, (17) *w;* $Pxn\text{-}GAL4^{8.1.1}$*, UAS-GFP* (Stramer et al., 2005), (18) *w[1118];* $P\{w[+mC]=UAS\text{-}lacZ.B\}Bg4\text{-}1\text{-}2$, (19) *Cg-GAL4;* $Atg1^{\Delta 3D}$*/TM6C Sb Tb* (derived from $Atg1^{\Delta 3D}$; Scott et al., 2004), and *w; UAS-IR*$mtm^{3.1}$*;* $Atg1^{\Delta 3D}$*/TM6C Sb Tb*.

### Determination of animal viability and lethal phase

For trans-heterozygous *mtm* mutants, first instar larvae were collected on grape juice agar plates 1 d after egg laying. Larvae were transferred to fresh plates supplemented with yeast paste and allowed to develop at 25°C. Viable larvae were counted each day up to 12 d after embryo laying. For RNAi hairpin–expressing flies, crosses were incubated at 25°C for 12 h to allow for sufficient egg laying, parents were removed, and progeny were allowed to develop in the vials at 29°C. The number of animals reaching pupal, pharate, and adult stages were counted for each WT and mutant genotype.

### Characterization of hemocytes

To test developmental timing for *mtm* requirement in hemocytes, experiments using the temperature sensitivity of GAL4 were performed on *Pxn-GAL4/UAS-lacZ* and *UAS-IR*$mtm^{3.1}$*/+; Pxn-GAL4/+* staged larvae reared either continuously at 18 or 29°C or raised at 18°C for 3 d after embryo collection then shifted to 29°C for 1 d. For hemocyte imaging (detailed in the following paragraph), hemocytes were bled from three to four wandering third instar larvae 4 d after egg laying into 100 µl complete medium (for live cell imaging) or PBS and were allowed to attach to a glass coverslip for 1 h at 25°C. Using bled hemocytes, a hemocytometer was used to determine cell numbers, and cell viability was determined using the Live/Dead Assay for Cell Viability kit (Invitrogen). To assess efficiency of RNAi knockdown in hemocytes, RT-PCR was performed on a population of primary hemocytes isolated to near purity from third instar larvae. For hemocyte purification, third instar larvae were washed with 70% ethanol then PBS. Approximately 150 mg wet WT larvae was used per preparation. The larvae were added to a cell strainer with a 70-µm nylon mesh placed in a shallow collecting dish and crushed with the back of an Eppendorf tube. The released hemocytes within the crude preparation were filtered through the 70-µm filter on the cell strainer into a 50-ml tube, and the crushed larvae were washed three times with PBS, pH 7.4. The hemocytes were centrifuged at 200 rpm for 5 min, and the supernatant containing the hemocytes collected centrifuged at 2,000 rpm for 10 min. The supernatant was discarded, and the collected hemocytes were used for mRNA extraction and RT-PCR as described for molecular analyses.

### Hemocyte wound recruitment assay and imaging of hemocytes in larvae

Wandering third instar larvae raised at 29°C were washed in PBS, briefly cleaned in 100% ethanol, and rinsed with PBS. The larvae were placed on a piece of paper to dry and mounted dorsal side up on a strip of double-sided tape fastened on a glass slide. Larvae were wounded in abdominal segment 5 or 6 using a Straight Stab pin (0.03-mm tip diameter; Fine Science Tools). Immediately after wounding, a drop of PBS was placed on the larvae to release them from the tape. The larvae recovered on standard grape agar plates for 6 h at 25°C, were briefly immobilized on ice, then remounted dorsal side up on double-sided tape. A glass coverslip (#1.5; 22-mm square) was placed on the larvae and attached with tape on two edges to minimize larval body wall contractions during imaging. Care was taken not to squash the larvae. The larvae were imaged with a 20× 0.5 NA objective (HC PL FLUOTAR; Leica) on a fluorescence microscope (DM1600; Leica). To estimate sessile hemocyte populations, wandering third instar larvae were mounted on double-sided tape and imaged. For each larva, images of GFP-positive hemocytes throughout abdominal segments 5 or 6 were collected and quantified.

### Cell staining and microscopy

For visualization of lysosomes, live cells were stained for 5 min with LysoTracker red DND-99 (1:7,500; Invitrogen) and Hoechst 33342 (1:1,000; Invitrogen) in complete medium, then washed and kept in complete medium for fluorescence microscopy at room temperature. Digital images of $Kc_{167}$ cells were taken on a microscope (Axiovert 200M; Carl Zeiss, Inc.) using a 63× 1.4 NA Plan Apo objective, transmission grid (ApoTome; Carl Zeiss, Inc.), and a camera (ORCA-ER; Hamamatsu Photonics). AxioVision software (Carl Zeiss, Inc.) was used for image acquisition and 3D reconstruction. Digital imaging of hemocytes was performed on a point-scanning microscope (FV1000; Olympus) controlled by the FluoView program (Olympus) using a 60× 1.2 NA Plan Apo N objective with 2× zoom. ImageJ (National Institutes of Health) was used for exporting tagged image file formats (TIFFs) and 3D reconstruction. For fluid phase uptake and trafficking, cells were given a 5-min pulse with dextran Alexa Fluor 488 (molecular mass, 10,000; 1 mg/ml; Invitrogen) together with LysoTracker red (1:10,000) and Hoechst (1:1,000) in complete Schneider's medium at room temperature. Cells were washed five times in PBS and chased in complete Schneider's medium for 20 min. Cells were imaged live with a microscope (Axiovert 200M). Similar experiments were performed using Alexa Fluor 488–conjugated BSA (Invitrogen). For assessment of bacterial engulfment and trafficking, hemocytes of genotypes *Pxn-GAL4/UAS-lacZ* and *UAS-IRmtm$^{3.1}$/+; UAS-IRmtm$^{3.5}$/Pxn-GAL4* dissected in Schneider's complete medium and allowed to spread for 30 min were given a pulse of fluorescein-labeled *E. coli* (Vybrant phagocytosis assay; Invitrogen) in PBS for 5 min, washed with PBS, and incubated for 1.5 h. Fluorescence of extracellular bacteria was quenched with Trypan blue for 5 min, washed in PBS for 5 min, and LysoTracker red and Hoechst were added before imaging with a microscope (Axiovert 200M) using a 63× objective and transmission grid (ApoTome). Photoshop (Adobe) was used to adjust the levels and curves and to crop and resize images.

For F-actin visualization and immunohistochemistry, hemocytes or $Kc_{167}$ cells were fixed for 10 min in 3.7% formaldehyde 1x PBS and washed twice for 5 min. PBST (PBS with 0.1% Triton X-100) was blocked for 10 min. PBSTB (PBST with 3% BSA) was stained overnight at 4°C with Alexa Fluor 546 phalloidin (1:100; Invitrogen), mouse anti–α-tubulin (1:500; Sigma-Aldrich), rabbit anti-Rab5 (1:50; Wucherpfennig et al., 2003), mouse anti-Golgi (1:200; EMD), or guinea pig anti-SCAR (1:100; Zallen et al., 2002) in PBSTB and for 1 h with Alexa Fluor secondary antibodies as needed (1:1,000; Invitrogen) in PBSTB, washed in PBS for 10 min, stained with DAPI for 10 min, and washed twice with PBS for 10 min. Cells were kept in PBS and visualized using fluorescence microscopy. Digital images were taken at room temperature either on an epifluorescence microscope (Axiovert 200M) or a point-scanning confocal microscope (FV1000) or using a 60x objective with a spinning-disk fluorescence microscope (DSU; Olympus) using a 60x 1.2 NA Plan Apo N objective and SlideBook software (Intelligent Imaging Innovations). Images were exported as 16-bit TIFFs using ImageJ. Photoshop was used to adjust the levels and curves and to crop and resize images.

### Time-lapse microscopy

For time-lapse imaging of cell morphology and dynamics, GFP-expressing hemocytes were imaged every 10 s for 5 min using a 60x 1.2 NA Plan Apo N objective on a spinning-disk fluorescence microscope (DSU). Time-lapse imaging of mCherry:2xFYVE or Pi3K68D:GFP and LysoTracker in hemocytes were obtained every 15 s for 5 min with three z sections spaced 0.3-µm apart at each time point on a point-scanning confocal microscope (FV1000) using a 60x 1.4 NA objective and 488- or 543-nm laser. Acquisition was performed with FluoView software, and image analysis was performed with ImageJ software. Time-lapse imaging of Pxn>GFP:Rab7 and LysoTracker red in hemocytes was captured every 10 s for 60 frames on a spinning-disk fluorescence microscope (DSU). TIFF files were exported as a video interleave file at three frames per second. Time-lapse imaging of Pi3K68D:GFP in $Kc_{167}$ cells was collected every 6 s (or 4 s with drug treatments) for 60 frames with an epifluorescence microscope (Axiovert 200M). TIFF files were exported as QuickTime files (Apple) at three frames per second. Photoshop and ImageJ were used for digital editing and production of time-lapse videos. Time-lapse microscopy imaging was performed at room temperature with cells in complete Schneider's media.

### Fixation, embedding, and transmission electron microscopy imaging

RNAi was performed in 100-mm Petri dishes. After 5 d, cells were harvested by centrifugation for fixation. Samples were immersed in modified Karnovsky's fixative (1.5% glutaraldehyde, 3% paraformaldehyde, and 2% sucrose in 0.1 M cacodylate buffer, pH 7.4) for 8 h, postfixed in 1% osmium tetroxide in 0.1 M cacodylate buffer for 1 h, and stained en bloc in 1% uranyl acetate for 1 h. Samples were dehydrated in ethanol, embedded in epoxy resin, sectioned at 60–70 nm, and picked up on Formvar- and carbon-coated copper grids. Grids were stained with uranyl acetate and lead nitrate, viewed using a transmission electron microscope (Philips CM-10; FEI), and photographed using a digital camera (Gatan).

### Generation of DNA constructs

Monomeric *mCherry* cDNA (Shaner et al., 2004) was inserted into pTW1129 tagless destination vector (provided by T. Murphy, Carnegie Institution, Baltimore, MD; *Drosophila* Gateway Vector Collection) upstream of the Gateway cassette to create pUAST-*mCherry-ccdB*. Full-length *mtm* cDNA was PCR amplified (*5′*-CACCATGGATCCCTCCGCG-3′ and *5′*-GTGCATAGGCGAGGCCAGA-3′), cloned into the pENTR/D-TOPO entry vector (Invitrogen), subcloned by an LR recombination reaction into Gateway destination vectors pTGW-1075 (UAS-*eGFP:mtm*) and pUAST-*mCherry-ccdB* (UAS-*mCherry:mtm*), and confirmed by sequencing and protein expression. EcoRI restriction digest of PCR-amplified full-length *mtm* cDNA (clone LD28822; *Drosophila* Genomics Resource Center [DGRC]) was subcloned to make UAST-*mtm:eGFP*. UAS-*GFP:mtm* and UAS-*FLAG:mtm* were generated from insertion of PCR-amplified full-length *mtm* cDNA into Gateway pENTR/D-TOPO and recombination into tag-containing destination vectors. The *mtm* cDNA mutation of codon 403 (CGC to TGC) was made using site-directed mutagenesis (QuickChange; Agilent Technologies). NotI restriction digest of human *GFP:MTMR2* (provided by J. Dixon, University of California, San Diego, La Jolla, CA) was subcloned into pUAST for UAS-*GFP:MTMR2*. Full-length *Pi3K68D* splice form A (clone LD28067; DGRC) was subcloned into pENTR1A vector (Invitrogen), excluding the STOP codon, to generate pENTR1A-*Pi3K68D* RA. LR recombination was performed with destination vectors pUAST-*ccdB-GFP* (*Drosophila* Gateway Vector Collection) and pUAST-*mCherry-ccdB* to obtain C- and N-terminally tagged *Pi3K68D:GFP* and *mCherry:Pi3K68D*, respectively. *myc:2XFYVE* was amplified from pUAST-*GFP:myc:2XFYVE* (provided by M. González-Gaitán, University of Geneva, Geneva, Switzerland) and inserted into pUAST-*mCherry* to generate pUAST-*mCherry:myc:2XFYVE*.

### Kc cell culture, DNA transfection, RNAi, and molecular analyses

*Drosophila* $Kc_{167}$ cells (Echalier and Ohanessian, 1969) were cultured in Schneider's *Drosophila* medium (Invitrogen) containing 10% FBS and 1% penicillin/streptomyocin (Sigma-Aldrich) at 24°C. Effectene transfection reagent (QIAGEN) was used for DNA delivery of metallothionein-*GAL4* along with the UAS constructs of interest, UAS-*GFP:Rab7*, UAS-*GFP:myc:2xFYVE* (provided by M. González-Gaitán), UAS-*GFP:LAMP* (provided by H. Krämer, University of Texas Southwestern, Dallas, TX), UAS-*mtm:GFP*, UAS-*GFP:mtm*, or UAS-*Pi3K68D:GFP*. To induce the metallothionein-*GAL4*, transfected cells were incubated with 0.75 mM $CuSO_4$ in complete media for 6–8 h before imaging. To test effects of cytoskeletal disruption on *mtm* RNAi phenotype or Pi3K68D localization and motility, cells were treated with 50 µM latrunculin B (EMD) for 2 h in complete medium or 15 µM nocodazole (Sigma-Aldrich) in PBS for 2 h and imaged live.

Double-stranded RNAs were generated from genomic DNA sequences, and RNAi for 3–5 d was performed as described previously (Kiger et al., 2003). To induce cellular elongation, cells were incubated 3 d after RNAi with a final concentration of 1 µM ecdysone (Sigma-Aldrich) in complete medium for 36 h before fixation. RNAi efficiency was determined from mRNA isolated from Trizol cell extracts and RT-PCR of cDNA (Invitrogen). Cell extracts in RIPA lysis buffer with protease inhibitor cocktail (Sigma-Aldrich) were used for Western blots with rabbit anti-GFP (1:2,000; Santa Cruz Biotechnology, Inc.), mouse anti–α-tubulin (1:5,000; Sigma-Aldrich), or mouse Ag10.2 anti-EcR (Developmental Studies Hybridoma Bank) followed by anti–rabbit HRP or anti–mouse HRP (1:10,000; Invitrogen).

To determine $Kc_{167}$ cell numbers after RNAi, control or *mtm* RNAi cells in poly-D-lysine–coated glass-bottom 96-well plates were incubated at 24°C for 4 d. After 3 d, some wells were treated with 1 µM ecdysone (Sigma-Aldrich) in complete medium for 24 h. Cells from each condition were imaged then scraped, resuspended in media, and counted by hemocytometer on d 1–4 after plating. To assess cell viability and relative cell size by flow cytometry, control and *mtm* RNAi-treated $Kc_{167}$ cells 4 d after plating with or without addition of 1 µM ecdysone for 18 h were scraped, filtered, and resuspended in PBS. Flow cytometric analysis of 20,000 ungated cells for forward and side scatter properties were collected from replicate samples from three experiments. A uniform gate drawn for forward and side scatter plots was applied to all samples collected in the same experiment and used to quantify the percentage of live and dead cells.

### Phosphatase activity assay

$Kc_{167}$ cells ($10^7$ cells/two 100-mm plates) transfected with UAS-*FLAG:mtm* or UAS-*FLAGmtm$^{R403C}$* and metallothionein-*GAL4* were induced 48 h later

with 1 mM $CuSO_4$ overnight. Plates were washed twice with ice-cold PBS and lysed in 500 µl lysis buffer (25 mM Tris-HCl, 1 mM EDTA, 0.1 mM EGTA, 5 mM $MgCl_2$, 150 mM NaCl, 10% glycerol, 1% NP-40, 1 mM DTT, and 1x protease inhibitor [Sigma-Aldrich]). Lysates were spun at 13,000 rpm for 10 min, the supernatant was collected, and equal volumes of cell lysates were immunoprecipitated using anti-Flag M2 agarose beads (Sigma-Aldrich) for 2 h at 4°C. Beads were washed three times with lysis buffer, once with lysis buffer without NP-40, twice in reaction buffer (20 mM Tris-HCl, pH 7.4, 5 mM $MgCl_2$, and 0.5 mM EDTA), and then split into four tubes (two used for PI(3)P and two used for PI(3,5)$P_2$). Phosphatase activity was measured using the malachite green assay (Echelon Biosciences, Inc.) following the manufacturer's instructions. Reaction mix (reaction buffer plus 50 µM PIPs) was added to each tube, incubated for 20 min at 25°C, then stopped by addition of 7 µl 0.05 mM $Na_3VO_4$ and heated at 95°C for 2 min. Free phosphate in solution was measured by plate reader. Beads were loaded onto a 4–12% SDS polyacrylamide gel (Invitrogen) to estimate the amount of immunoprecipitated protein. The gel was stained with Sypro Ruby red stain (Invitrogen), and it was found that the Mtm-WT and Mtm-R403C amounts were equal.

**Radiolabeling, extraction, and quantification of PI(3)P concentrations**

After 3 d of RNAi, $Kc_{167}$ cells were labeled for 40 h with 90 µCi/ml myo-[2-$^3$H]inositol (PerkinElmer) in inositol-free Schneider's *Drosophila* medium (Invitrogen). Cells were scraped in PBS and collected by centrifugation. Phosphoinositides were extracted as described previously (Rudge et al., 2004), and the dried extracts were analyzed by HPLC as described previously (Baird et al., 2008). Radiolabeled phospholipids from yeast extracts were used as standards.

**Statistical analysis**

The area of subcellular objects (Rab5, GFP:Rab7, and LysoTracker) were scored and quantified using either AxioVision or CellProfiler software. Images were thresholded, segmented, and measured in marker channel to determine object areas and in nuclei channel to determine total cell count. Per object measurements for ≥745 compartments from ≥60 cells pooled from at least two experiments were analyzed with Prism software (GraphPad Software, Inc.) to determine object area mean, standard error, and Student's *t* test, and results were converted from pixels to squared micrometers for Figs. 4 (H and I), 5 C, 8 (C–D'), S2 G, and S3 D. Colocalization of dextran and LysoTracker was scored and quantified with the MetaMorph software (MDS Analytical Technologies) colocalization module per entire field and reported as percentage of dextran versus LysoTracker overlap in Fig. 5 (A and A'). The area of localized PI(3)P per cell was determined using AxioVision software. Images were thresholded, segmented, and measured for field area of GFP:2xFYVE channel and DAPI channel to count nuclei, then used to calculate normalized GFP:2xFYVE area per cell per field. Prism software was used to calculate the mean-normalized GFP:2xFYVE area from 8–13 fields (31–88 cells) across two experiments, standard error, and Student's *t* test for Fig. 7 C. Cell morphology of F-actin–labeled spread hemocytes or GFP-positive transfected $Kc_{167}$ cells was assessed manually and categorized for all detectable cells within entire image fields (≥12) from three experiments, and results were plotted as the mean percentage of total scored cells for Figs. 1 G and 2 G. Prism was used to calculate SD and Student's *t* test.

Transmission electron microscopy data in Fig. 4 (M and P) were quantified from 26 cells selected randomly for each condition, with the only criteria that the entire cell with nucleus cross section was represented. The cell perimeter and secondary lysosomes, as visually identified by membrane whorls, were manually outlined in Photoshop. The total area of secondary lysosomes as a percentage of the entire cell area was calculated in Excel (Microsoft), analyzed in Prism with Student's *t* test, and graphed as a scatter plot with mean percent cell area. Electron-lucent membrane structures were visually identified, and the number of single-membrane–bound and double-membrane–bound structures were counted for each cell. Prism software was used to determine Student's *t* test and graph results as a scatter plot with the mean number of structures per cell.

Hemocytometer counts of bled hemocytes were made independently from 10 larvae. CellProfiler software was used to estimate sessile hemocyte populations per segment from images of GFP-positive hemocytes in abdominal segments 5 or 6 from10 larvae. Images of wound sites from ≥11 larvae per genotype were analyzed in Photoshop by manually counting hemocytes within one-wound diameter. Prism software was used to calculate mean, standard error, and Student's *t* test for hemocyte numbers graphed in Fig. 3 (A, C, and F). Hemocytometer counts of RNAi-treated $Kc_{167}$ cells from three experiments were used to calculate mean, SD, and Student's *t* test for Fig. 1 D. Percentage of live and dead cells, for 20,000 cells for each of two experiments, and forward scatter from four experiments, each of 16,000 gated cells, were used to calculate mean, standard error, and Student's *t* test for Fig. S2 (C and D). Phosphatase activities were analyzed for mean, standard error, and Student's *t* test from four experiments for Fig. 6 A. Mean percent radiolabeled PI(3)P and Student's *t* test were calculated from two experiments.

**Online supplemental material**

Fig. S1 shows results from Kc cell RNAi screen. Fig. S2 demonstrates normal cell number, viability, and ecdysone reception in *mtm* RNAi Kc cells. Fig. S3 shows normal phagocytosis in *mtm*-depleted hemocytes, dependence of *mtm* RNAi lysosomal defects on HOPS complex, and that *Fab1* RNAi shares similar lysosomal but not morphology defects. Fig. S4 shows GFP:2xFYVE-altered distribution in Kc cells and hemocytes and the affect of Pi3K functions on hemocyte protrusions. Table S1 displays adult viability and visible phenotypes detected with tissue-targeted *mtm* depletion and genetic interactions. Video 1 shows time-lapse microscopy of altered cortical dynamics in *mtm*-depleted hemocytes. Video 2 shows time-lapse microscopy of fusion between mCherry:2xFYVE compartments with lack of tubulation in *mtm*-depleted hemocytes. Video 3 shows time-lapse microscopy of GFP:Rab7 and LysoTracker in hemocytes. Video 4 shows time-lapse microscopy of Pi3K68D:GFP motility and association with LysoTracker compartments. Online supplemental material is available at http://www.jcb.org/cgi/content/full/jcb.200911020/DC1.

We are grateful to T. Neufeld, M. González-Gaitán, H. Kramer, M. Galko, J. Dixon, H. Stenmark, J. Zallen, Bloomington *Drosophila* Stock Center, and Vienna *Drosophila* RNAi Center for reagents. We thank C. Garza, J. Dennis, G. Kim, K. Lau, and S. Cox for technical assistance. We thank B. Wakimoto and C. Zuker for *mtm*$^{22-4747}$ alleles. We thank T. Meerloo for technical assistance with electron microscopy and M. Farquhar for use of the Center for Molecular Medicine Electron Microscope Facility. We are grateful to S. Emr for the use of HPLC instrumentation. Microscopy was performed in part at the University of California San Diego Neuroscience Microscopy Shared Imaging Facility.

This work was supported by a Fonds de la Recherche en Santé du Québec (to S. Jean), the National Institutes of Health (grant DK17780), the Kimmel Foundation (grant KF06-120), the Packard Foundation (grant 2005-29096 to A.A. Kiger), and the University of California San Diego Neuroscience Microscopy Shared Imaging Facility (grant P30 NS047101).

Submitted: 3 November 2009
Accepted: 14 July 2010

## References

Asha, H., I. Nagy, G. Kovacs, D. Stetson, I. Ando, and C.R. Dearolf. 2003. Analysis of Ras-induced overproliferation in *Drosophila* hemocytes. *Genetics.* 163:203–215.

Babcock, D.T., A.R. Brock, G.S. Fish, Y. Wang, L. Perrin, M.A. Krasnow, and M.J. Galko. 2008. Circulating blood cells function as a surveillance system for damaged tissue in *Drosophila* larvae. *Proc. Natl. Acad. Sci. USA.* 105:10017–10022. doi:10.1073/pnas.0709951105

Baird, D., C. Stefan, A. Audhya, S. Weys, and S.D. Emr. 2008. Assembly of the PtdIns 4-kinase Stt4 complex at the plasma membrane requires Ypp1 and Efr3. *J. Cell Biol.* 183:1061–1074. doi:10.1083/jcb.200804003

Banta, L.M., J.S. Robinson, D.J. Klionsky, and S.D. Emr. 1988. Organelle assembly in yeast: characterization of yeast mutants defective in vacuolar biogenesis and protein sorting. *J. Cell Biol.* 107:1369–1383. doi:10.1083/jcb.107.4.1369

Berger, P., S. Bonneick, S. Willi, M. Wymann, and U. Suter. 2002. Loss of phosphatase activity in myotubularin-related protein 2 is associated with Charcot-Marie-Tooth disease type 4B1. *Hum. Mol. Genet.* 11:1569–1579. doi:10.1093/hmg/11.13.1569

Bolino, A., M. Muglia, F.L. Conforti, E. LeGuern, M.A. Salih, D.M. Georgiou, K. Christodoulou, I. Hausmanowa-Petrusewicz, P. Mandich, A. Schenone, et al. 2000. Charcot-Marie-Tooth type 4B is caused by mutations in the gene encoding myotubularin-related protein-2. *Nat. Genet.* 25:17–19. doi:10.1038/75542

Cao, C., J. Laporte, J.M. Backer, A. Wandinger-Ness, and M.P. Stein. 2007. Myotubularin lipid phosphatase binds the hVPS15/hVPS34 lipid kinase complex on endosomes. *Traffic.* 8:1052–1067. doi:10.1111/j.1600-0854.2007.00586.x

Cao, C., J.M. Backer, J. Laporte, E.J. Bedrick, and A. Wandinger-Ness. 2008. Sequential actions of myotubularin lipid phosphatases regulate endosomal PI(3)P and growth factor receptor trafficking. *Mol. Biol. Cell.* 19:3334–3346. doi:10.1091/mbc.E08-04-0367

Cooper, J.L., B.J. Till, and S. Henikoff. 2008. Fly-TILL: reverse genetics using a living point mutation resource. *Fly (Austin).* 2:300–302.

Di Paolo, G., and P. De Camilli. 2006. Phosphoinositides in cell regulation and membrane dynamics. *Nature.* 443:651–657. doi:10.1038/nature05185

Dietzl, G., D. Chen, F. Schnorrer, K.C. Su, Y. Barinova, M. Fellner, B. Gasser, K. Kinsey, S. Oppel, S. Scheiblauer, et al. 2007. A genome-wide transgenic RNAi library for conditional gene inactivation in *Drosophila*. *Nature.* 448:151–156. doi:10.1038/nature05954

Domin, J., L. Harper, D. Aubyn, M. Wheeler, O. Florey, D. Haskard, M. Yuan, and D. Zicha. 2005. The class II phosphoinositide 3-kinase PI3K-C2beta regulates cell migration by a PtdIns3P dependent mechanism. *J. Cell. Physiol.* 205:452–462. doi:10.1002/jcp.20478

Echalier, G. 1997. *Drosophila* Cells in Culture. Academic Press, New York. 702 pp.

Echalier, G., and A. Ohanessian. 1969. [Isolation, in tissue culture, of *Drosophila melangaster* cell lines]. *C. R. Acad. Sci. Hebd. Seances Acad. Sci. D.* 268:1771–1773.

Entchev, E.V., A. Schwabedissen, and M. González-Gaitán. 2000. Gradient formation of the TGF-beta homolog Dpp. *Cell.* 103:981–991. doi:10.1016/S0092-8674(00)00200-2

Falasca, M., and T. Maffucci. 2007. Role of class II phosphoinositide 3-kinase in cell signalling. *Biochem. Soc. Trans.* 35:211–214. doi:10.1042/BST0350229

Falasca, M., W.E. Hughes, V. Dominguez, G. Sala, F. Fostira, M.Q. Fang, R. Cazzolli, P.R. Shepherd, D.E. James, and T. Maffucci. 2007. The role of phosphoinositide 3-kinase C2alpha in insulin signaling. *J. Biol. Chem.* 282:28226–28236. doi:10.1074/jbc.M704357200

Fili, N., V. Calleja, R. Woscholski, P.J. Parker, and B. Larijani. 2006. Compartmental signal modulation: endosomal phosphatidylinositol 3-phosphate controls endosome morphology and selective cargo sorting. *Proc. Natl. Acad. Sci. USA.* 103:15473–15478. doi:10.1073/pnas.0607040103

Gillooly, D.J., I.C. Morrow, M. Lindsay, R. Gould, N.J. Bryant, J.M. Gaullier, R.G. Parton, and H. Stenmark. 2000. Localization of phosphatidylinositol 3-phosphate in yeast and mammalian cells. *EMBO J.* 19:4577–4588. doi:10.1093/emboj/19.17.4577

Gonzalez-Gaitan, M. 2008. The garden of forking paths: recycling, signaling, and degradation. *Dev. Cell.* 15:172–174. doi:10.1016/j.devcel.2008.07.001

Grant, B.D., and J.G. Donaldson. 2009. Pathways and mechanisms of endocytic recycling. *Nat. Rev. Mol. Cell Biol.* 10:597–608. doi:10.1038/nrm2755

Hafen, E. 2004. Cancer, type 2 diabetes, and ageing: news from flies and worms. *Swiss Med. Wkly.* 134:711–719.

Jahn, R., T. Lang, and T.C. Südhof. 2003. Membrane fusion. *Cell.* 112:519–533. doi:10.1016/S0092-8674(03)00112-0

Johannes, L., and V. Popoff. 2008. Tracing the retrograde route in protein trafficking. *Cell.* 135:1175–1187. doi:10.1016/j.cell.2008.12.009

Juhász, G., J.H. Hill, Y. Yan, M. Sass, E.H. Baehrecke, J.M. Backer, and T.P. Neufeld. 2008. The class III PI(3)K Vps34 promotes autophagy and endocytosis but not TOR signaling in *Drosophila*. *J. Cell Biol.* 181:655–666. doi:10.1083/jcb.200712051

Kadandale, P., J.D. Stender, C.K. Glass, and A.A. Kiger. 2010. Conserved role for autophagy in Rho1-mediated cortical remodeling and blood cell recruitment. *Proc. Natl. Acad. Sci. USA.* 107:10502–10507. doi:10.1073/pnas.0914168107

Kiger, A.A., B. Baum, S. Jones, M.R. Jones, A. Coulson, C. Echeverri, and N. Perrimon. 2003. A functional genomic analysis of cell morphology using RNA interference. *J. Biol.* 2:27. doi:10.1186/1475-4924-2-27

Kihara, A., T. Noda, N. Ishihara, and Y. Ohsumi. 2001. Two distinct Vps34 phosphatidylinositol 3–kinase complexes function in autophagy and carboxypeptidase Y sorting in *Saccharomyces cerevisiae*. *J. Cell Biol.* 152:519–530. doi:10.1083/jcb.152.3.519

Kim, S.A., G.S. Taylor, K.M. Torgersen, and J.E. Dixon. 2002. Myotubularin and MTMR2, phosphatidylinositol 3-phosphatases mutated in myotubular myopathy and type 4B Charcot-Marie-Tooth disease. *J. Biol. Chem.* 277:4526–4531. doi:10.1074/jbc.M111087200

Lanot, R., D. Zachary, F. Holder, and M. Meister. 2001. Postembryonic hematopoiesis in *Drosophila*. *Dev. Biol.* 230:243–257. doi:10.1006/dbio.2000.0123

Laporte, J., L.J. Hu, C. Kretz, J.L. Mandel, P. Kioschis, J.F. Coy, S.M. Klauck, A. Poustka, and N. Dahl. 1996. A gene mutated in X-linked myotubular myopathy defines a new putative tyrosine phosphatase family conserved in yeast. *Nat. Genet.* 13:175–182. doi:10.1038/ng0696-175

Laporte, J., F. Blondeau, A. Buj-Bello, D. Tentler, C. Kretz, N. Dahl, and J.L. Mandel. 1998. Characterization of the myotubularin dual specificity phosphatase gene family from yeast to human. *Hum. Mol. Genet.* 7:1703–1712. doi:10.1093/hmg/7.11.1703

Laporte, J., F. Blondeau, A. Gansmuller, Y. Lutz, J.L. Vonesch, and J.L. Mandel. 2002. The PtdIns3P phosphatase myotubularin is a cytoplasmic protein that also localizes to Rac1-inducible plasma membrane ruffles. *J. Cell Sci.* 115:3105–3117.

Lee, Y.S., and R.W. Carthew. 2003. Making a better RNAi vector for *Drosophila*: use of intron spacers. *Methods.* 30:322–329. doi:10.1016/S1046-2023(03)00051-3

Lindmo, K., and H. Stenmark. 2006. Regulation of membrane traffic by phosphoinositide 3-kinases. *J. Cell Sci.* 119:605–614. doi:10.1242/jcs.02855

MacDougall, L.K., J. Domin, and M.D. Waterfield. 1995. A family of phosphoinositide 3-kinases in *Drosophila* identifies a new mediator of signal transduction. *Curr. Biol.* 5:1404–1415. doi:10.1016/S0960-9822(95)00278-8

MacDougall, L.K., M.E. Gagou, S.J. Leevers, E. Hafen, and M.D. Waterfield. 2004. Targeted expression of the class II phosphoinositide 3-kinase in *Drosophila melanogaster* reveals lipid kinase-dependent effects on patterning and interactions with receptor signaling pathways. *Mol. Cell. Biol.* 24:796–808. doi:10.1128/MCB.24.2.796-808.2004

Maffucci, T., F.T. Cooke, F.M. Foster, C.J. Traer, M.J. Fry, and M. Falasca. 2005. Class II phosphoinositide 3-kinase defines a novel signaling pathway in cell migration. *J. Cell Biol.* 169:789–799. doi:10.1083/jcb.200408005

Mima, J., and W. Wickner. 2009. Phosphoinositides and SNARE chaperones synergistically assemble and remodel SNARE complexes for membrane fusion. *Proc. Natl. Acad. Sci. USA.* 106:16191–16196. doi:10.1073/pnas.0908694106

Mosesson, Y., G.B. Mills, and Y. Yarden. 2008. Derailed endocytosis: an emerging feature of cancer. *Nat. Rev. Cancer.* 8:835–850. doi:10.1038/nrc2521

Norris, F.A., and P.W. Majerus. 1994. Hydrolysis of phosphatidylinositol 3,4-bisphosphate by inositol polyphosphate 4-phosphatase isolated by affinity elution chromatography. *J. Biol. Chem.* 269:8716–8720.

Palamidessi, A., E. Frittoli, M. Garré, M. Faretta, M. Mione, I. Testa, A. Diaspro, L. Lanzetti, G. Scita, and P.P. Di Fiore. 2008. Endocytic trafficking of Rac is required for the spatial restriction of signaling in cell migration. *Cell.* 134:135–147. doi:10.1016/j.cell.2008.05.034

Parrish, W.R., C.J. Stefan, and S.D. Emr. 2005. PtdIns(3)P accumulation in triple lipid-phosphatase-deletion mutants triggers lethal hyperactivation of the Rho1p/Pkc1p cell-integrity MAP kinase pathway. *J. Cell Sci.* 118:5589–5601. doi:10.1242/jcs.02649

Ridley, A.J. 2006. Rho GTPases and actin dynamics in membrane protrusions and vesicle trafficking. *Trends Cell Biol.* 16:522–529. doi:10.1016/j.tcb.2006.08.006

Robinson, F.L., and J.E. Dixon. 2006. Myotubularin phosphatases: policing 3-phosphoinositides. *Trends Cell Biol.* 16:403–412. doi:10.1016/j.tcb.2006.06.001

Rudge, S.A., D.M. Anderson, and S.D. Emr. 2004. Vacuole size control: regulation of PtdIns(3,5)P2 levels by the vacuole-associated Vac14-Fig4 complex, a PtdIns(3,5)P2-specific phosphatase. *Mol. Biol. Cell.* 15:24–36. doi:10.1091/mbc.E03-05-0297

Rusten, T.E., L.M. Rodahl, K. Pattni, C. Englund, C. Samakovlis, S. Dove, A. Brech, and H. Stenmark. 2006. Fab1 phosphatidylinositol 3-phosphate 5-kinase controls trafficking but not silencing of endocytosed receptors. *Mol. Biol. Cell.* 17:3989–4001. doi:10.1091/mbc.E06-03-0239

Saftig, P., and J. Klumperman. 2009. Lysosome biogenesis and lysosomal membrane proteins: trafficking meets function. *Nat. Rev. Mol. Cell Biol.* 10:623–635. doi:10.1038/nrm2745

Schu, P.V., K. Takegawa, M.J. Fry, J.H. Stack, M.D. Waterfield, and S.D. Emr. 1993. Phosphatidylinositol 3-kinase encoded by yeast VPS34 gene essential for protein sorting. *Science.* 260:88–91. doi:10.1126/science.8385367

Scott, R.C., O. Schuldiner, and T.P. Neufeld. 2004. Role and regulation of starvation-induced autophagy in the *Drosophila* fat body. *Dev. Cell.* 7:167–178. doi:10.1016/j.devcel.2004.07.009

Seals, D.F., G. Eitzen, N. Margolis, W.T. Wickner, and A. Price. 2000. A Ypt/Rab effector complex containing the Sec1 homolog Vps33p is required for homotypic vacuole fusion. *Proc. Natl. Acad. Sci. USA.* 97:9402–9407. doi:10.1073/pnas.97.17.9402

Shaner, N.C., R.E. Campbell, P.A. Steinbach, B.N. Giepmans, A.E. Palmer, and R.Y. Tsien. 2004. Improved monomeric red, orange and yellow fluorescent proteins derived from *Discosoma* sp. red fluorescent protein. *Nat. Biotechnol.* 22:1567–1572. doi:10.1038/nbt1037

Simonsen, A., and S.A. Tooze. 2009. Coordination of membrane events during autophagy by multiple class III PI3-kinase complexes. *J. Cell Biol.* 186:773–782. doi:10.1083/jcb.200907014

Simonsen, A., A.E. Wurmser, S.D. Emr, and H. Stenmark. 2001. The role of phosphoinositides in membrane transport. *Curr. Opin. Cell Biol.* 13:485–492. doi:10.1016/S0955-0674(00)00240-4

Soldati, T., and M. Schliwa. 2006. Powering membrane traffic in endocytosis and recycling. *Nat. Rev. Mol. Cell Biol.* 7:897–908. doi:10.1038/nrm2060

Srivastava, S., Z. Li, L. Lin, G. Liu, K. Ko, W.A. Coetzee, and E.Y. Skolnik. 2005. The phosphatidylinositol 3-phosphate phosphatase myotubularin-related protein 6 (MTMR6) is a negative regulator of the Ca2+-activated

K+ channel KCa3.1. *Mol. Cell. Biol.* 25:3630–3638. doi:10.1128/MCB.25.9.3630-3638.2005

Srivastava, S., L. Di, O. Zhdanova, Z. Li, S. Vardhana, Q. Wan, Y. Yan, R. Varma, J. Backer, H. Wulff, et al. 2009. The class II phosphatidylinositol 3 kinase C2beta is required for the activation of the K+ channel KCa3.1 and CD4 T-cells. *Mol. Biol. Cell.* 20:3783–3791. doi:10.1091/mbc.E09-05-0390

Stramer, B., W. Wood, M.J. Galko, M.J. Redd, A. Jacinto, S.M. Parkhurst, and P. Martin. 2005. Live imaging of wound inflammation in *Drosophila* embryos reveals key roles for small GTPases during in vivo cell migration. *J. Cell Biol.* 168:567–573. doi:10.1083/jcb.200405120

Sunio, A., A.B. Metcalf, and H. Krämer. 1999. Genetic dissection of endocytic trafficking in *Drosophila* using a horseradish peroxidase-bride of sevenless chimera: hook is required for normal maturation of multivesicular endosomes. *Mol. Biol. Cell.* 10:847–859.

Taylor, G.S., T. Maehama, and J.E. Dixon. 2000. Inaugural article: myotubularin, a protein tyrosine phosphatase mutated in myotubular myopathy, dephosphorylates the lipid second messenger, phosphatidylinositol 3-phosphate. *Proc. Natl. Acad. Sci. USA.* 97:8910–8915. doi:10.1073/pnas.160255697

Tosch, V., H.M. Rohde, H. Tronchère, E. Zanoteli, N. Monroy, C. Kretz, N. Dondaine, B. Payrastre, J.L. Mandel, and J. Laporte. 2006. A novel PtdIns3P and PtdIns(3,5)P2 phosphatase with an inactivating variant in centronuclear myopathy. *Hum. Mol. Genet.* 15:3098–3106. doi:10.1093/hmg/ddl250

Tsujita, K., T. Itoh, T. Ijuin, A. Yamamoto, A. Shisheva, J. Laporte, and T. Takenawa. 2004. Myotubularin regulates the function of the late endosome through the gram domain-phosphatidylinositol 3,5-bisphosphate interaction. *J. Biol. Chem.* 279:13817–13824. doi:10.1074/jbc.M312294200

Vergne, I., E. Roberts, R.A. Elmaoued, V. Tosch, M.A. Delgado, T. Proikas-Cezanne, J. Laporte, and V. Deretic. 2009. Control of autophagy initiation by phosphoinositide 3-phosphatase Jumpy. *EMBO J.* 28:2244–2258. doi:10.1038/emboj.2009.159

Vicinanza, M., G. D'Angelo, A. Di Campli, and M.A. De Matteis. 2008. Function and dysfunction of the PI system in membrane trafficking. *EMBO J.* 27:2457–2470. doi:10.1038/emboj.2008.169

Wen, P.J., S.L. Osborne, I.C. Morrow, R.G. Parton, J. Domin, and F.A. Meunier. 2008. Ca2+-regulated pool of phosphatidylinositol-3-phosphate produced by phosphatidylinositol 3-kinase C2alpha on neurosecretory vesicles. *Mol. Biol. Cell.* 19:5593–5603. doi:10.1091/mbc.E08-06-0595

Williams, M.J. 2007. *Drosophila* hemopoiesis and cellular immunity. *J. Immunol.* 178:4711–4716.

Wucherpfennig, T., M. Wilsch-Bräuninger, and M. González-Gaitán. 2003. Role of *Drosophila* Rab5 during endosomal trafficking at the synapse and evoked neurotransmitter release. *J. Cell Biol.* 161:609–624. doi:10.1083/jcb.200211087

Wurmser, A.E., and S.D. Emr. 1998. Phosphoinositide signaling and turnover: PtdIns(3)P, a regulator of membrane traffic, is transported to the vacuole and degraded by a process that requires lumenal vacuolar hydrolase activities. *EMBO J.* 17:4930–4942. doi:10.1093/emboj/17.17.4930

Xie, Z., and D.J. Klionsky. 2007. Autophagosome formation: core machinery and adaptations. *Nat. Cell Biol.* 9:1102–1109. doi:10.1038/ncb1007-1102

Xue, Y., H. Fares, B. Grant, Z. Li, A.M. Rose, S.G. Clark, and E.Y. Skolnik. 2003. Genetic analysis of the myotubularin family of phosphatases in *Caenorhabditis elegans*. *J. Biol. Chem.* 278:34380–34386. doi:10.1074/jbc.M303259200

Yoshioka, K., N. Sugimoto, N. Takuwa, and Y. Takuwa. 2007. Essential role for class II phosphoinositide 3-kinase alpha-isoform in Ca2+-induced, Rho- and Rho kinase-dependent regulation of myosin phosphatase and contraction in isolated vascular smooth muscle cells. *Mol. Pharmacol.* 71:912–920. doi:10.1124/mol.106.032599

Zallen, J.A., Y. Cohen, A.M. Hudson, L. Cooley, E. Wieschaus, and E.D. Schejter. 2002. SCAR is a primary regulator of Arp2/3-dependent morphological events in *Drosophila*. *J. Cell Biol.* 156:689–701. doi:10.1083/jcb.200109057

Zhao, Y., I. Gaidarov, and J.H. Keen. 2007. Phosphoinositide 3-kinase C2alpha links clathrin to microtubule-dependent movement. *J. Biol. Chem.* 282:1249–1256. doi:10.1074/jbc.M606998200

Zou, W., Q. Lu, D. Zhao, W. Li, J. Mapes, Y. Xie, and X. Wang. 2009. *Caenorhabditis elegans* myotubularin MTM-1 negatively regulates the engulfment of apoptotic cells. *PLoS Genet.* 5:e1000679. doi:10.1371/journal.pgen.1000679